Influence of Surface Pretreatments on Composition, Structure and Corrosion Performance of Zirconium Conversion Coating Applied to AA7075-T6

Journal of The Electrochemical Society, 2025 **172** 111501

Influence of Surface Pretreatments on Composition, Structure and Corrosion Performance of Zirconium Conversion Coating Applied to AA7075-T6

Gavrilo Šekularac,[1,a,*] Janez Kovač,[2] and Ingrid Milošev[1,*,z]

[1] *Jožef Stefan Institute, Department of Physical and Organic Chemistry, SI-1000 Ljubljana, Slovenia*
[2] *Jožef Stefan Institute, Department of Surface Engineering, SI-1000 Ljubljana, Slovenia*

The effect of chemical pretreatment of aluminium alloy 7075-T6 on the composition, morphology, and structure of zirconium conversion coatings (ZrCC) was investigated. Chemical pretreatments included: (i) alkaline etching and desmutting using commercial reagents, (ii) alkaline etching using sodium hydroxide, (iii) acidic etching using nitric acid, (iv) desmutting using a commercial reagent and boiling in deionised water, and (v) alkaline etching and desmutting using nitric acid. ZrCCs were deposited at room temperature from a 200 ppm H_2ZrF_6 solution of pH 4.8. A commercial SurTec® coating containing zirconium and trivalent chromium was used as a benchmark. The electrochemical behaviour was evaluated using potentiodynamic polarisation measurements and electrochemical impedance spectroscopy conducted over a minimum of 5 days and up to 15 days in 0.1 M NaCl. Corrosion resistance was further assessed through immersion testing. Microstructural characterisation was performed using scanning electron microscopy with energy-dispersive spectroscopy, X-ray photoelectron spectroscopy, and time-of-flight secondary ion mass spectrometry. The SurTec® pretreatment of AA7075-T6 activated the self-sealing of the subsequently deposited ZrCC, about 40 nm thick, which exhibited the highest degree of compactness and uniformity. This study showed a significant impact of surface chemical pretreatment on the microstructural and protective properties of ZrCCs deposited on 7075 alloy.
 [DOI: 10.1149/1945-7111/ae18fd]

Manuscript submitted August 20, 2025; revised manuscript received October 28, 2025. Published November 10, 2025.

Supplementary material for this article is available online

Aluminium alloy (AA) 7075-T6 is a high-performance material renowned for its exceptional mechanical properties, particularly its high strength-to-weight ratio and fatigue resistance.[1] With a typical yield strength of approximately 500 MPa (72,000 psi), it is among the strongest commercially available AAs. The Al matrix contains zinc (5.6–6.1 wt%), magnesium (2.1–2.5 wt%), and copper (1.2–1.6 wt%), along with minor contents of chromium (0.18%–0.28 wt%) and trace elements. AA7075 is widely utilised in aerospace, automotive, defence, sports equipment, and marine industries. However, the alloy exhibits moderate corrosion resistance, which limits its performance in harsh environments.[2–4] Namely, alloying elements contribute to the formation of intermetallic particles (IMPs) that exhibit a cathodic nature relative to the Al matrix, rendering it more susceptible to localised degradation mechanisms.[5–8] To enhance its corrosion resistance, the material requires appropriate surface pretreatment, such as conversion coating or anodisation, followed by the application of organic coatings.[9–12]

Chemical conversion coatings (CCCs), especially chromate and phosphate CCs, have long been employed across various industrial sectors;[9,13–16] however, due to their adverse environmental and health impacts, chromate coatings have been banned in the EU and USA, while phosphate coatings are being phased out in favour of greener and more economical alternatives.[17] Among these alternatives, zirconium conversion coatings (ZrCCs) and trivalent chromium processing (TCP) have emerged as promising solutions.[9,18–34]

ZrCCs are commonly formed via an electrochemical process in baths containing hexafluorozirconic acid (H_2ZrF_6); in industrial applications, organic and inorganic additives are also added.[9,35–46] The process involves dissolving the natural oxide layer on the substrate with free fluoride ions, exposing cathodic sites where oxygen reduction and hydrogen evolution occur, causing a localised increase in pH and thus facilitating the precipitation of zirconium oxide and the subsequent formation of the coating.[44,47–50] ZrCCs have garnered significant attention due to their simplicity, cost-effectiveness, multi-metal nature and ability to enhance substrate adhesion and corrosion resistance.[9,34,51–55] While anodised layers, which are thicker and offer superior corrosion protection, are preferred for applications requiring exceptional durability (e.g., in aerospace), ZrCCs provide an economical alternative for industries such as automotive and appliances, where such rigorous protection is not always necessary.

Before deposition of conversion coatings, AAs require chemical cleaning and activation. This process involves a sequence of alkaline or acidic cleaning, followed by alkaline or acidic etching and acid desmutting.[56–67] The alkaline cleaning step effectively removes contaminants and residual oils from manufacturing and storage. Subsequently, the etching and desmutting stages modify the AA surface, enhancing its uniformity and compactness to improve the performance of the conversion coating. Alkaline etching of AA7075-T6 at pH 11.6, followed by desmutting in nitric acid (HNO_3), resulted in preferential dissolution of Mg and surface enrichment with Cu.[59] Commercial treatment, including degreasing at pH 8.3 and nitric acid desmutting, results in lesser Cu enrichment. It was reported that an alkaline degreasing agent (pH = 9.1) effectively removed Mg, leaving a 10 nm-thick Al_2O_3 film.[68] In contrast, alkaline activation using NaOH or Na_2CO_3 solutions (pH = 13) resulted in the formation of a significantly thicker oxide layer (40–60 nm), primarily composed of $Mg(OH)_2$ or $MgCO_3$.[68]

Several studies have investigated the effects of chemical pretreatment on the surface characteristics of various AAs and their influence on the conversion coating process and overall performance, as summarised in the following text.

Recently, the effects of alkaline etching of AA2024-T3 in 1 M NaOH and acid pickling in a solution containing 30% HNO_3 and 10% acetic acid on the microstructure, ZrCC's deposition and performance were systematically investigated.[56] Desmutting in HNO_3 induced trenching around Al_2CuMg IMPs, which may be deleterious for ZrCC performance. In contrast, desmutting in acetic acid enhanced surface activation, without inducing trenching around IMPs. However, non-uniform deposition over Cu-rich IMPs was identified as a limiting factor for the coating's corrosion protection effectiveness. Alkaline etching in NaOH facilitated the removal of larger IMPs and increased the deposition rate of ZrCC, but it also led

*Electrochemical Society Member.
[a] Present Address: Institute of Chemistry, Technology and Metallurgy, Department of Electrochemistry, 11000 Belgrade, Serbia.
[z] E-mail: ingrid.milosev@ijs.si

to a mud-cracking morphology and inadequate adhesion.[56] Alkaline etching of AA2024-T3 was reported to effectively eliminate IMPs; however, it also induces surface copper enrichment, facilitating Cu incorporation into the TCP coating, thereby compromising overall corrosion resistance.[69] It was further documented that the morphology of Al-Cu-Fe-Mn IMPs remained largely unchanged upon chemical pretreatment of AA2024; however, trenching was observed at the θ-Al_2Cu/Al interface, while Al_2CuMg IMPs underwent severe corrosion and the formation of Cu remnants.[70] Although the Cu enrichment facilitated ZrCC formation, it also promoted nanopores and cracks within the ZrCC.[70]

Among series 6xxx, the effects of alkaline cleaning and acid desmutting using HNO_3 and a mixture of HNO_3 and HF on the protection performance of ZrCC-coated AA6061 were investigated.[71] An optimal pretreatment should induce relatively slow initiation of ZrCC deposition at the cathodic sites, followed by lateral growth at the matrix. The addition of HF in the desmutting solution induced dealloying of IMPs and was detrimental to the ZrCC deposition.[71] For AA6014, it was reported that acidic (30 s in 30 vol% nitric acid), alkaline (3 min in a 3 vol% potassium hydroxide at 57 °C), and pseudoboehmite (15 s in boiling deionised water) treatments led to the exposure and dealloying of Cu-containing IMPs in AA6014, thus creating preferential nucleation sites for ZrCC formation.[72,73] The hydroxyl fraction was recognised as the critical factor for achieving high ZrCC coverage. Thermal and acid treatment resulted in lower hydroxyl fractions. In contrast, alkaline and pseudoboehmite, with higher hydroxyl fractions, achieved higher ZrCC coverage and better adhesion of the top epoxy layer.[72,73] In contrast, for AA1050, which lacks Cu-containing IMPs, alkaline pretreatment was identified as a critical factor for effective ZrCC deposition.[74]

Alkaline cleaning of AA7075-T6 resulted in the formation of a 50 nm thick, dark oxide layer consisting mainly of Al hydroxide.[75] Subsequent desmutting in HNO_3 effectively removed the majority of the oxide layer. Additionally, $MgSi_2$ second-phase particles were transformed into SiO_2, while Al-Fe-Cu particles underwent corrosion and dealloying, leading to the redeposition of Cu particles and the trenching formation.[75] The dissolution and deposition behaviour of Cu and Mg from Al-3 at%Mg, Al-3 at%Cu, and AA7449-T651 was studied in a nitro-sulpho-ferric acid solution. Acid pickling selectively dissolved Cu and Mg from the alloys, significantly reducing their subsequent dissolution during the conversion process.[76] ZrCC formed in the presence of NO_3^- added to the bath, resulted in thinner, more homogeneous Zr-oxide layers, whereas the F^--based bath led to the formation of thicker, more complex oxides.[76]

Most existing studies have focused on the effects of pretreatment on microstructural modifications and processes such as dealloying, redeposition, and trenching. However, only a limited number have examined the correlation between pretreatment effects and the electrochemical behaviour of ZrCCs using potentiodynamic and electrochemical impedance measurements.[56,63,69,71,77] As a substrate, AA2024[56,63,69] was mainly explored, with fewer reports on the 6xxx[71] and 7xxx series.[77] Further, among the conversion coatings, various types were studied, i.e., ZrCC,[56] TCP,[63,69] ZrCC containing phosphate ions,[71] and commercial ZrCC coated with an organic coating.[77] In this study, we systematically investigated the influence of various pretreatments on the microstructure of ZrCCs applied to AA7075-T6, as well as their impact on electrochemical behaviour and self-sealing/self-healing performance. Notably, potentiodynamic measurements alone are not suitable for assessing self-sealing or self-healing properties, nor for evaluating long-term corrosion protection, as these effects may be overlooked.[12,22] We have therefore complemented the potentiodynamic measurements with long-term electrochemical impedance spectroscopy, as in our previous studies.[22,23,34,41,58,78]

In our previous work, we showed that ZrCCs provide excellent corrosion protection for AA3005 and A356.0, as well as very good protection for alloys 1050 A, 380.0, and 5754. However, they do not provide adequate corrosion protection for AA2024 and AA7075 due to the detrimental effects of Cu and Zn-based IMPs present in these alloys.[34,58,78] ZrCCs showed a strong self-sealing/self-healing effect when applied on AA3005, AA3003 and A356.0, while this effect was weak for alloys 1050A, 380.0, and 5754, and it did not occur for AA2024 and AA7075.[78] We hypothesised that with proper surface pretreatment and cleaning of AA7075 and AA2024, ZrCCs could provide improved corrosion protection and self-sealing/self-healing effect also on these alloys.

This study aimed to investigate the influence of various pretreatment methods (as outlined in Table I) on the formation and corrosion behaviour of ZrCCs applied to AA7075-T6. To achieve this, a combination of microstructural characterisation techniques, electrochemical methods and immersion tests was utilised. As a benchmark, TCP coating was used. In our forthcoming study, we will present the effect of chemical pretreatment of AA2024-T3 on the corrosion performance of subsequently deposited ZrCCs.

Experimental

Materials, sample preparation and chemicals.—Aluminium alloy 7075-T6/EN AW-7075/EN AW-AlZn5.5MgCu/UNS-A97075 alloy with composition: Zn 5.81 wt%, Mg 2.55 wt%, Fe 0.21 wt%, Si 0.08 wt%, Cu 1.67 wt%, and Al remainder. It was produced by Kaiser Aluminum in the form of a 1 mm-thick sheet. Samples used in experiments were cut into a square shape with dimensions of 3 cm × 3 cm.

Only the sample designated as MP underwent mechanical pretreatment by grinding with SiC papers ranging from 320- to 4000-grit, using a grinding/polishing machine LaboPol-20 (Struers, Ballerup, Denmark). Immediately after grinding, samples were ultrasonicated in absolute ethanol for 5 min using an ultrasonic bath Elmasonic P (Elma, Germany) at 37 kHz and 100% power.

The following chemicals were used for experiments: NaCl (for analysis, Fischer Scientific, Leicestershire), NaOH (reagent grade, ⩾98.0%, pellets, Sigma-Aldrich, Saint Louis, USA), HNO_3 (conc. 65% in H_2O, reagent grade, Sigma-Aldrich, Saint Louis, USA), H_3PO_4 (conc. 85% in H_2O, reagent grade, Sigma-Aldrich, Saint Louis, USA), SurTec 061® (alkaline cleaner composed of phosphates and tetraborates ingredients, pH = 9.0 at 20 g L^{-1}), SurTec 089® (detergent booster consisting of nonionic surfactants, pH = 9.8 at 2 vol%), SurTec 181® (alkaline etcher composed of polyalcohols and NaOH, pH = 12.5 at 10 g L^{-1}), SurTec 496® (acid desmutter composed of HNO_3, H_2SO_4 and HF, pH <1), SurTec 650® (chromitAL TCP, trivalent chromium passivation composed of trivalent chromium salts, pH = 2.9–4), SurTec 650 A® (additive for trivalent chromium passivation composed of methacryl-amidopropyl-trimethylammoniumchloride, ethyl acrylate and acrylic acid, polymer 1%–3%; metilizotiazolinon 0,0015%-0.1%; 1,2-Benzizotiazol-3(2H)-on <0.05%), H_2ZrF_6 (50 wt% in water, Sigma-Aldrich, Saint Louis, USA), NH_4HCO_3 (reagent grade, Sigma-Aldrich, Steinheim, Germany). Milli-Q Direct water with a resistivity of 18.2 MΩ·cm at 25 °C (Merck, Darmstadt, Germany) was used for rinsing and solution preparation.

pH was measured using a pH meter 827 pH-lab equipped with Unitrode/Pt1000 (Metrohm AG, Herisau, Switzerland). Teflon beakers (V = 1 L) were used for conversion and desmutting baths, while glass beakers (V = 600 ml) were used for all other baths. Sample holders were made of polyethylene. Conversion coating solutions were stored in polyethylene bottles.

Chemical pretreatments.—As-received samples were subject to CPs, as presented in Table I. The steps of CPs are given in consecutive order from left to right, with preparation details including concentration, pH, temperature, procedure duration, and stirring.

CP0 denotes the acetone-cleaned sample only. All other CPs included CP0 as the first step.

CP1 – CP3 comprise commercial SurTec® pretreatments with CP1, including degreasing, alkaline etching, and desmutting, CP2

Table I. Chemical pretreatments of AA7075 (steps are given in consecutive order from left to right). RT is the room temperature.

Treatment steps	Solvent clean	Commercial treatment SurTec®			Desmuting	Alkaline treatments					Acidic treatments			Pseudo-boehmite treatment
		Degreasing	Etching	Desmutting		A1	A2	A3	A4	A5	AC1	AC2	AC3	PB
Ingredients	Acetone	5 Vol % SurTec 061 + 0.5 Vol % SurTec 089	5 Vol.% SurTec 181	20 Vol % SurTec 496	HNO_3	42 g/L NaOH + H_3PO_4	NaOH	NaOH	NaOH	NaOH	HNO_3	HNO_3	HNO_3	H_2O
pH	/	9	12.5	1.2	1.2	11	9	10	11	12	1	2	3	7
T, ∘C	/	60	50	RT	RT	60	60	60	60	60	RT	RT	RT	100
t, min	5	10	1.5	15	15	3	3	3	3	3	3	3	3	1
Stirring	/	/	/	Yes	Yes	/	/	/	/	/	/	/	/	/
CP0	Yes													
CP1	Yes	Yes	Yes	Yes										
CP2	Yes	Yes												
CP3	Yes	Yes	Yes											
CP4	Yes	Yes								Yes				
CP5	Yes	Yes							Yes					
CP6	Yes	Yes						Yes						
CP7	Yes	Yes					Yes							
CP8	Yes	Yes				Yes								
CP9	Yes	Yes	Yes	Yes										Yes
CP10	Yes	Yes											Yes	
CP11	Yes	Yes										Yes		
CP12	Yes	Yes									Yes			
CP13	Yes	Yes	Yes		Yes									

only degreasing, and CP3 degreasing and alkaline etching. Degreasing proceeded for 10 min at pH = 9 at 60 °C, alkaline etching for 1.5 min at pH = 12.5 at 50 °C and desmutting for 15 min at pH = 1.2 at room temperature (RT).

CP4 − CP8 comprise SurTec® degreasing and alkaline treatments for 3 min at 60 °C using NaOH only (CP4 − CP7, pH = 12, 11, 10 and 9, respectively) and NaOH and H_3PO_4 (CP8, pH = 11).

CP9 comprised SurTec® degreasing, alkaline etching and desmutting, followed by pseudoboehmite treatment for 1 min of boiling in water at pH = 7. Compared to CP1, it includes the additional pseudoboehmite step.

CP10 − CP12 include SurTec® degreasing and acid treatment using HNO_3 for 3 min at pH = 3, 2, and 1, respectively, at room temperature.

CP13 denotes commercial SurTec® pretreatments including degreasing and alkaline etching, followed by desmutting using HNO_3 for 3 min at pH = 1.2 at room temperature. It differs from CP1 in terms of the desmutting solution.

After each step, samples were rinsed by immersion in a Milli-Q Direct water bath for 1 min; the only exception was the desmutting process, after which they were rinsed twice in separate consecutive Milli-Q Direct water baths for 1 min each.

The coated AA7075 samples were designated according to their chemical pretreatments and coating types, i.e. from CP0-ZrCC to CP13-ZrCC for the ZrCC-coated samples and CP1-TCP for the TCP-coated sample.

Preparation of conversion coatings.—Before the application of conversion coating, as-received samples (without mechanical pretreatment) were chemically pretreated by commercial and non-commercial chemical pretreatments (CPs), as shown in Table I. Immediately following the CP, samples were washed off with Milli-Q Direct water and then rinsed by dipping twice in Milli-Q Direct water baths for 1 min, followed by dipping in a conversion bath for 5 min. The zirconium conversion bath contained $1{\cdot}10^{-3}$ mol L^{-1} (200 ppm) of H_2ZrF_6. pH was set to 4.8 using 15 wt% NH_4HCO_3. The conversion process was carried out at room temperature without stirring. The samples were afterwards rinsed with Milli-Q Direct water and washed off by dipping in a Milli-Q Direct water bath for 1 min. The samples were then dried with an N_2 stream and left to dry in the air for 24 h.

For comparative purposes, we prepared trivalent chromium SurTec650/650 A® chromitAL coating containing Zr and trivalent chromium (TCP). The recommended commercial process consisted of commercial chemical pretreatment (CP1) and successive immersion for 5 min in a conversion bath containing a mixture of 20 vol% SurTec 650® and 5 vol% SurTec 650 A®. The pH of the solution was adjusted to 3.9 using 15 wt% NH_4HCO_3. All other procedure parameters were the same as for the ZrCCs.

Immersion test.—Samples were immersed in a 250 ml 0.1 M NaCl solution for 14 days in accordance with NACE TM0169/G31–12a standard.[79] Samples were placed in electrochemical flat cells made of plexiglass (V = 250 ml) with an exposed area of 1 cm^2. Images of the samples after 14 days of immersion were captured with a 13 MP digital camera.

Electrochemical characterisation.—Electrochemical experiments were carried out with a Multi Autolab/M204 (Metrohm Autolab, Utrecht, Netherlands) potentiostat/galvanostat controlled by Nova 2.1 software. Measurements were conducted in a standard three-electrode flat cell with a 250 ml volume. The sample was the working electrode, a carbon rod was the counter electrode, and a saturated $Ag/AgCl_{(sat)}$ electrode was the reference electrode (E_{SHE} = 0.198 V). All potentials in the text refer to the $Ag/AgCl_{(sat)}$ scale. The electrolyte was a freshly prepared 0.1 M NaCl. The area of the working electrode was 1 cm^2. All measurements were conducted at room temperature.

Before electrochemical measurements, the sample was allowed to rest at open-circuit potential (OCP) for 1 h. Electrochemical measurements were conducted in the following sequence from least destructive to more destructive: (i) measurement of the OCP as a function of resting time, (ii) recording of linear polarisation resistance (LPR) curves, and (iii) recording of potentiodynamic polarisation (PDP) curves. The system was allowed to rest for 10 s before switching to the following electrochemical technique.

LPR curves were run in the range –10 to 10 mV vs OCP using a 0.1 mV s^{-1} scan rate. Polarisation resistance ($R_{p,LPR}$) was determined as the slope of the fitted potential (E) vs current density (j) curve using Nova 2.1 software.

PDP curves were recorded in the potential range starting at −250 mV vs the OCP in an anodic direction until the current density reached 0.1 mA cm^{-2}. The scan rate was 1 mV s^{-1}.

Corrosion current density (j_{corr}) and corrosion potential (E_{corr}) were determined using Nova 2.1 software based on the Tafel extrapolation method. Polarisation resistance was calculated from parameters obtained with the Tafel extrapolation ($R_{p,\ Tafel}$) method, using Nova 2.1 software based on Eq. 1 in accordance with standard ASTM G59–97.[80]

$$R_{p,Tafel} = \frac{B}{j_{corr}} \quad [1]$$

where B is the Stern-Geary constant.

Electrochemical impedance spectroscopy (EIS) spectra were recorded from 100 kHz to 5 mHz frequency using an AC potential amplitude of 10 mV (root-mean-square). Spectra were recorded at the OCP every day up to 5 days of immersion.

Electrochemical measurements were repeated for each condition for at least three different samples. Representative measurements are presented in plots, and average values with standard deviation are given in Tables SI–SIII. Average values are also provided in plots (e.g. for $|Z|_{5mHz}$ and OCP), when indicated.

Microstructural characterisation.—Scanning electron microscopy (SEM) images were taken in secondary electron (SE) and back-scattered (BSE) modes using an FEI Helios Nanolab 650 microscope. Energy-dispersive X-ray spectra (EDS) were taken using an Oxford Instruments AZtec system with an X-max SDD (50 mm^2) detector. The analysed area was 100 nm^2 with an analysis depth of 100 nm (near-surface condition) at a beam acceleration voltage of 3 kV. Before analysis, the samples were coated with a thin carbon layer to reduce the charging effect.

Time-of-flight secondary ion mass spectrometry (ToF-SIMS) ion depth profiles were made using the ToF-SIMS V spectrometer (ION TOF GmbH—Munster, Germany). The analysis chamber was operated at a pressure below $\sim 10^{-9}$ mbar. Depth profiles for negative ions were recorded by interlacing a pulsed 30 keV Bi^+ primary ion source delivering 1.2 pA target current over a 100 × 100 μm^2 area with sputtering using a 2 keV Cs^+ source beam delivering 523 nA target current over a 400 × 400 μm^2 area. The sputtering rate for ToF-SIMS depth profiling was determined by depth profiling of a thin film of Al_2O_3 of known thickness (50 nm) on a Si substrate under the same conditions as those applied for other samples. The sputtering rate was 0.30 nm s^{-1} (±0.02 nm s^{-1}).

X-ray photoelectron spectroscopy (XPS) was carried out using a PHI-TFA XPS spectrometer (Physical Electronics Inc.). The vacuum during the XPS analysis was in the range of 10^{-9} mbar. The analysed area was 0.4 mm in diameter, and the depth was 3−5 nm; X-rays were provided from a monochromatic Al Kα source at a photon energy of 1486.6 eV. The XPS spectrometer was nominally operated at an energy resolution of 0.6 eV measured on the Ag $3d_{5/2}$ peak. XPS spectra were analysed by Multipack software, version 8.0 (Physical Electronics Inc.). The position of the binding energies of the experimental spectra was aligned relative to the position of the C 1s peak at 284.8 eV.

Results

Electrochemical impedance spectroscopy.—The influence of CPs on the electrochemical behaviour of ZrCC applied to AA7075 was studied using EIS over five days of immersion in 0.1 M NaCl (Figs. 1, S1–S5 and Table SI). Corrosion resistance, self-sealing effect, and active corrosion protection of ZrCCs can be evaluated from the impedance modulus at low frequency of 5 mHz, which is approximately equal to the total polarisation resistance ($|Z|_{5mHz} \approx R_p$). Values of $|Z|_{5mHz}$ during prolonged immersion in 0.1 M NaCl for ZrCC-coated samples after various CPs are presented in Figs. 1 and S1 and Tables SI and SII. Commercial CP1 provided the most significant improvement in the corrosion protection performance of ZrCC applied to AA7075 (Fig. 1). This surface pretreatment activated the self-sealing/self-healing corrosion protection behaviour of ZrCC. Namely, during the first 3 days of immersion, CP1-ZrCC showed self-sealing behavior, which manifested itself by an increase of $|Z|_{5mHz}$ from $7.4{\cdot}10^5$ $\Omega{\cdot}cm^2$ to $4.7{\cdot}10^6$ $\Omega{\cdot}cm^2$ (Fig. 1). After 4 days, $|Z|_{5mHz}$ of CP1-ZrCC decreased down to $3.5{\cdot}10^6$ $\Omega{\cdot}cm^2$ indicating that pitting occurred; however, after this drop, $|Z|_{5mHz}$ recovered and reached value of $4.3{\cdot}10^6$ $\Omega{\cdot}cm^2$ on 5th day of immersion indicating that active corrosion protection occurred. Afterwards, $|Z|_{5mHz}$ of CP1-ZrCC remained stable around $4.4{\cdot}10^6$ $\Omega{\cdot}cm^2$ until the 12th day of immersion when it dropped down to $3.2{\cdot}10^6$ $\Omega{\cdot}cm^2$, indicating that pitting occurred again. The sample, however, recovered and reached a value of $4.4{\cdot}10^6$ $\Omega{\cdot}cm^2$ on the 14th day of immersion.

The average OCP of chemically pretreated ZrCC-coated and MP-7075 samples during immersion in 0.1 M NaCl solution is presented in Table SII and Fig. S6. The OCP of most ZrCC coatings applied after subsequent pretreatments stabilised within the range of –0.60 V to –0.70 V after 1 h. Throughout the immersion period, the OCP remained stable or exhibited a slight decrease. An exception was observed in the CP4-ZrCC sample, which displayed a significantly lower OCP after 1 h of immersion. This behaviour is attributed to the aggressive alkaline etching pretreatment, which exposed a substantial content of pure Mg and Al at the surface (see below). After 1 day of immersion, these elements likely dissolved or transformed into hydroxides, raising the OCP to –0.66 V. Subsequently, the CP4-ZrCC OCP remained stable throughout the immersion period. The CP1-ZrCC, applied after commercial pretreatment, exhibited an OCP of –0.60 V after 1 h of immersion. Over time, it remained stable within the range of –0.60 V to –0.65 V. Compared with the MP-7075 sample, the OCP of CP1-ZrCC was consistently more positive during immersion. The commercial TCP conversion coating exhibited an initial OCP of –0.65 V after 1 h of immersion. After 1 day, the potential decreased to –0.76 V, then gradually increased to –0.70 V over the remaining immersion period. The OCP of the CP1-TCP coating was more negative than that of the CP1-ZrCC and MP-7075 samples.

Results in Fig. 1 and Table SI show that CP1-ZrCC performed very close to CP1-TCP, but the latter outperformed the former. The standard deviation of impedance modulus values was greater for CP1-ZrCC than for CP1-TCP (Fig. S1), particularly on days associated with pitting events. This suggests that the TCP coating exhibited slightly superior performance, with a lower likelihood of pitting occurrence.

CP13 was identical to commercial CP1, except it used concentrated HNO_3 desmutter instead of the commercial one. The concentration, pH, and process parameters (pH, time, and temperature) of the HNO_3 desmutter were adjusted to match those in the commercial process. The corrosion protection performance of CP13-ZrCC was inferior to that of CP1-ZrCC, indicating that desmutting is a critical step of the chemical pretreatment before applying ZrCC.

CP9 was the modification of commercial CP1 with one additional step after desmutting; immersion of the CP1-ZrCC sample in boiling deionised water for 1 min to form a pseudoboehmite layer before the conversion coating process. This additional step significantly reduced the corrosion performance of ZrCC compared to CP1 (Fig. 1). Both CP9-ZrCC and CP13-ZrCC showed an increase of $|Z|_{5mHz}$ during 5 days of immersion in 0.1 M NaCl solution. The values of $|Z|_{5mHz}$ for CP9-ZrCC were twice as high as those of CP13-ZrCC. However, this was probably due to the formation of more uniform and compact corrosion products of aluminium hydrated oxide during immersion.

Other chemical pretreatments showed much worse corrosion protection performance than CP1, CP9 and CP13 (Figs. 1, Figs. S2–S5 and Table SI). Therefore, based on the criterion of high values of $|Z|_{5mHz} \approx R_p$, the following ranking of corrosion resistance is postulated: CP1-TCP ≈ CP1-ZrCC >> CP9-ZrCC > CP13-ZrCC > CP11-ZrCC. ZrCCs prepared using other CPs exhibited substantially lower corrosion resistance.

Immersion test.—We performed an immersion test in 0.1 M NaCl solution to visually evaluate the effect of chemical pretreatments on the corrosion performance of ZrCCs and TCP (Fig. 2). After 14 days of immersion, no visible damage was observed on TCP. The CP1-ZrCC sample suffered only very little damage in the form of a single pit. On CP9-ZrCC, there were four visible pits; on CP13-ZrCC, there were five visible pits with larger corroded areas than on CP9-ZrCC. The remaining samples were largely corroded, suggesting that these pretreatments did not improve the ZrCC

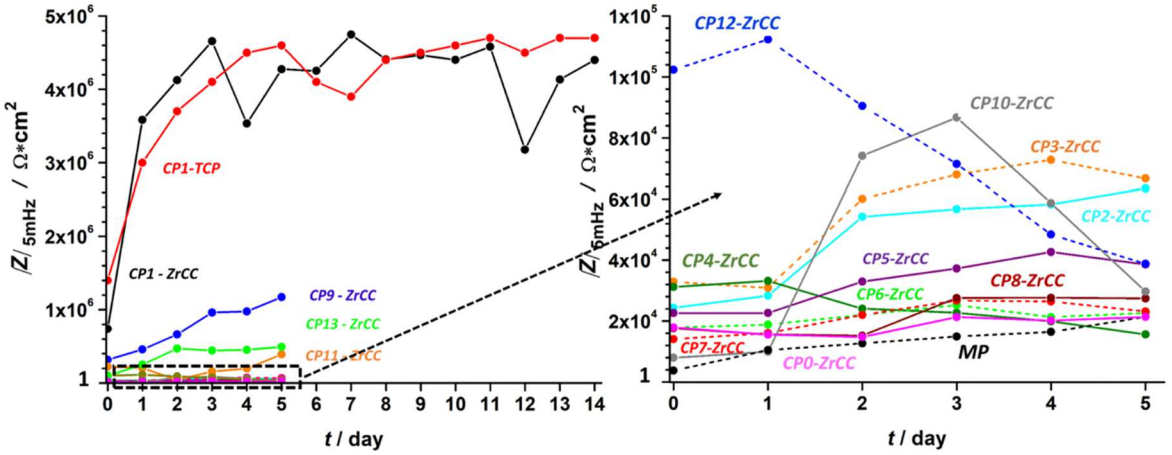

Figure 1. The average impedance modulus at 5 mHz ($|Z|_{5mHz}$) as a function of immersion time in 0.1 M NaCl solution for: mechanically pretreated (MP) AA7075, ZrCC-coated AA7075 and TCP-coated AA7075samples. Before ZrCC and TCP deposition, samples were subjected to chemical pretreatments CP0–CP13 (Table I). Original EIS spectra (representative measurement of several repetitions) are shown in Figs. S2-S5. Average data of $|Z|_{5mHz}$ and OCP and standard deviations are provided in Fig. S1 and Tables SI and SII. The enlarged y-scale is shown on the right.

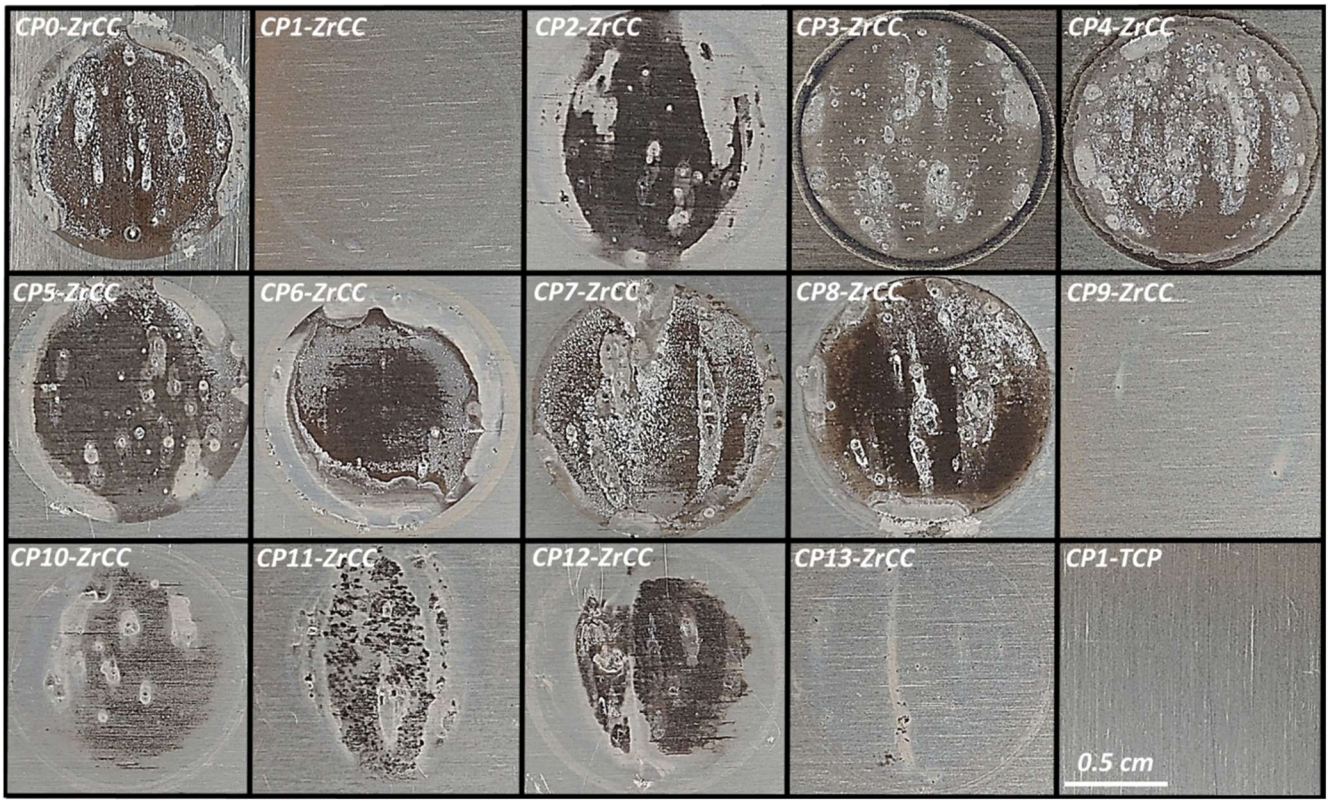

Figure 2. Images of ZrCC- and TCP-coated AA7075 samples after 14 days of immersion in 0.1 M NaCl solution. Before ZrCC and TCP deposition, samples were subjected to chemical pretreatments CP0–CP13 (Table I).

performance. The immersion test showed that the best improvement in corrosion properties was achieved after the commercial surface pretreatment CP1, followed by CP9 and CP13; the remaining pretreatments did not bring any improvements.

Based on the ranking on corrosion performance assessed by EIS measurements (Fig. 1) and immersion test (Fig. 2), we selected the following ZrCC-coated samples for further investigations: (i) sample exhibiting the highest corrosion resistance (CP1-ZrCC), (ii) sample prepared using a modified commercial CP incorporating an additional pseudoboehmite formation step (CP9-ZrCC), and (iii) sample prepared using a modified commercial CP, except with HNO_3 employed as the desmutting agent instead of the commercial desmutting agent (CP13-ZrCC). Furhermore, several other samples were selected to address the effect of individual pretreatment steps: (iv) the bare, untreated sample serving as a reference (CP0), (v) CP2-ZrCC subjected only to degreasing, (vi), CP4-ZrCC subjected to strong alkaline etching (pH = 12), (vii) CP8-ZrCC subjected to alkaline etching with phosphates in solution (pH = 11) and (viii) CP11-ZrCC subjected to degreasing and acid etching. These samples were further evaluated using potentiodynamic measurements and microstructural characterisation to systematically assess the impact of different pretreatment steps on corrosion resistance and surface characteristics.

Electrochemical potentiodynamic curves.—Potentiodynamic polarisation curves recorded in 0.1 M NaCl for CP-ZrCCs deposited on AA7075 samples are presented in Fig. 3. Also, curves recorded for MP AA7075 and CP1-TCP-coated samples are given. Electrochemical data deduced from the PDP curves are presented in Table SIII.

The corrosion resistance of ZrCCs applied on AA7075 after various chemical pretreatments, based on electrochemical data (small j_{corr}, large R_p), was in the following order: CP1-ZrCC >> CP13-ZrCC ≈ CP11-ZrCC > CP9-ZrCC > CP0-ZrCC > CP2-ZrCC > CP8-ZrCC > CP4-ZrCC.

The CP4-ZrCC subjected to prior strong alkaline etching exhibited a large passive window ($\Delta E = 0.56$ V). However, the j_{corr} for this pretreatment was the highest, indicating the formation of a thick and porous aluminium oxide/hydroxide layer during alkaline etching. Furthermore, the E_{corr} of CP4-ZrCC shifted to −1.14 V, compared to −0.65 V for CP0-ZrCC, indicating increased electrochemical activity and inadequate corrosion protection due to the porous nature of the coating. In contrast, ZrCCs applied after other CPs exhibited E_{corr} between −0.6 V and −0.65 V.

The highest corrosion resistance was achieved with the commercial SurTec® pretreatment (CP1-ZrCC), which closely matched the corrosion resistance of the CP1-TCP. Notably, CP1-ZrCC exhibited superior cathodic inhibition, surpassing even CP1-TCP, suggesting that the commercial pretreatment enhanced ZrCC's protective properties. However, CP1-ZrCC did not exhibit passive protection (enlarged image in Fig. 3b), and the current density increased abruptly above E_{corr}. CP1-TCP demonstrated a short range of 50 mV above E_{corr}, where the rise in current density was slowed down. Electrochemical data suggest that after 1 h of immersion, the ZrCCs primarily affected the cathodic process by reducing the cathodic current density but did not enhance passivity. However, with prolonged immersion, the situation is not as straightforward. The ZrCCs initially act as cathodic inhibitors by blocking cathodic sites. As the coating thickens and spreads throughout the matrix, it blocks the anodic dissolution and acts as an anodic inhibitor.[23,58,78]

SEM-EDS characterisation of chemically pretreated AA7075.—SEM SE, and BSE images of CP AA7075 samples after immersion for 14 days in 0.1 M NaCl (Fig. 2) are presented in Figs. 4, 5 and S7. The corresponding average compositions determined by EDS analyses are given in Table II. EDS analysis was performed at a beam voltage of 3 kV, corresponding to a 100 nm analysis depth (near-surface condition). EDS analysis was carried out to determine the elemental composition of the surface. It was not very detailed because the microstructure of AA7075 is well known, and we

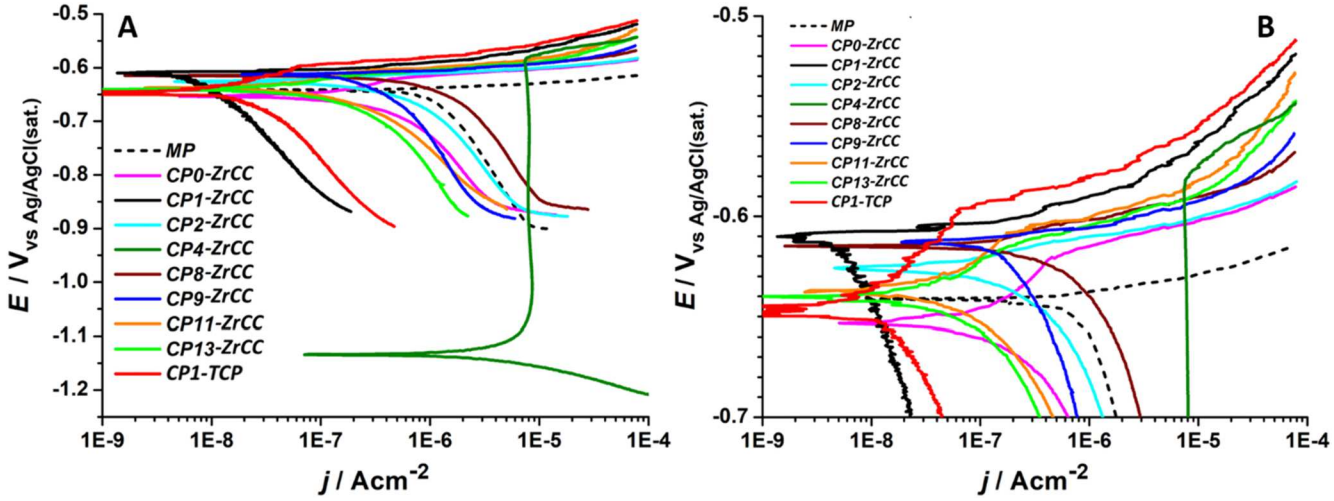

Figure 3. (A) Potentiodynamic polarisation curves, recorded in 0.1 M NaCl, for mechanically pretreated (MP) AA7075, ZrCC-coated AA7075 and TCP-coated AA7075 samples. Before ZrCC and TCP deposition, samples were subjected to chemical pretreatments CP0–CP13 (Table I). The TCP-coated sample served as a benchmark. Samples were rested at the OCP for 1 h before electrochemical measurement. Electrochemical data deduced from polarisation curves are given in Table SIII. (B) The enlarged y-scale is from −0.7 V to −0.5 V.

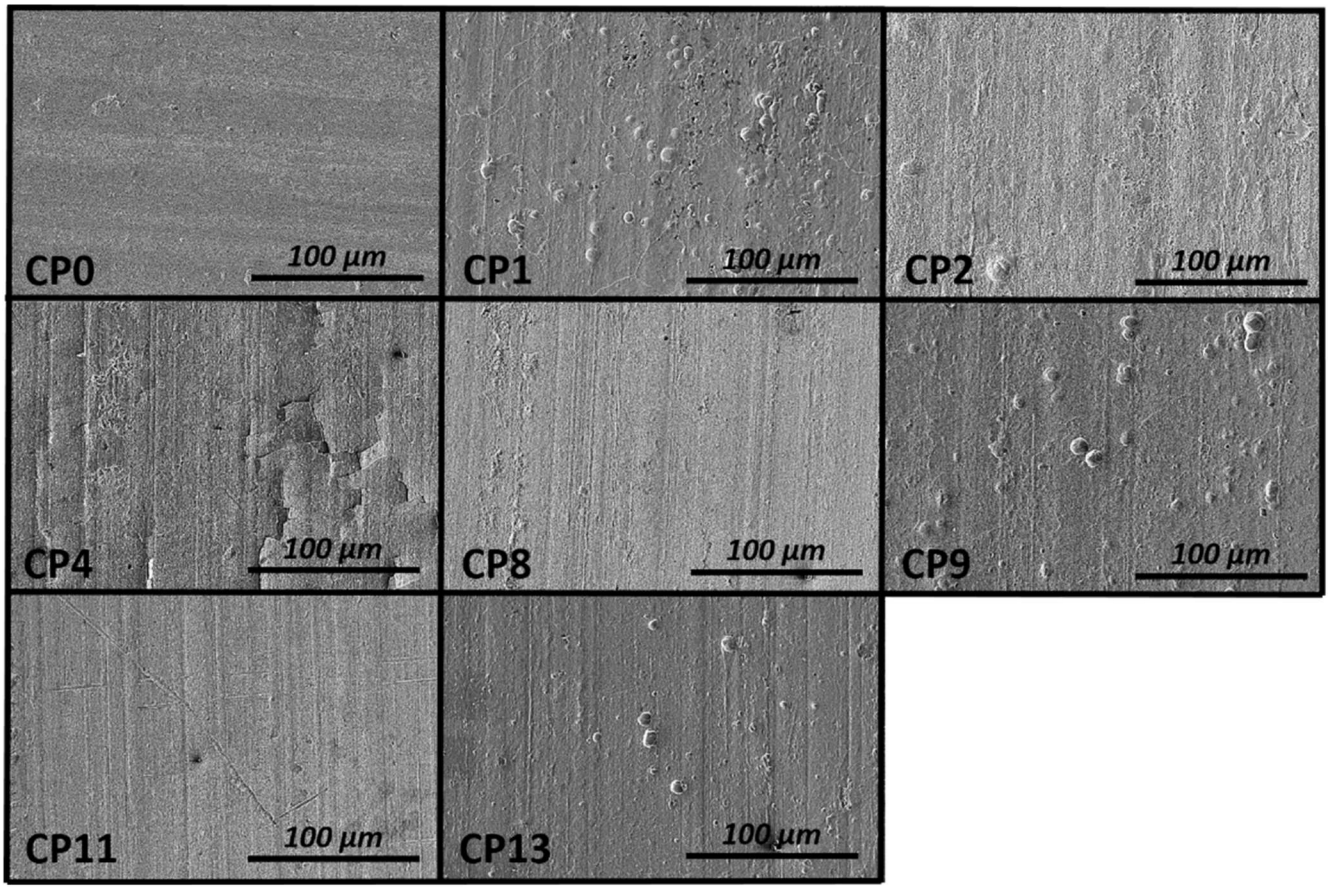

Figure 4. SEM-SE images (500 × magnification) of AA7075 samples after different chemical pretreatments (Table I). EDS analysis of the samples is presented in Table II.

focused only on general features.[5,6,75,81] SE-SEM images of lower magnifications (Fig. 4) show that commercial CP1 removed natural aluminium oxide, exposed grain boundaries and produced a significant content of nanometric globular deposits at the AA7075 surface. Similar surface morphology was observed for CP9 and CP13, except that grain boundaries were not visible.

CP4, including a strong alkaline etching after the degreasing step, produced a heavily damaged, cracked surface. The remaining CPs (CP2, CP8 and CP11) showed surface morphologies similar to that of the CP0 sample. BSE-SEM images (Fig. S7) showed the same surface morphology as SE-SEM images, with even better visibility of grain boundaries at the AA7075 surface after commercial CP1.

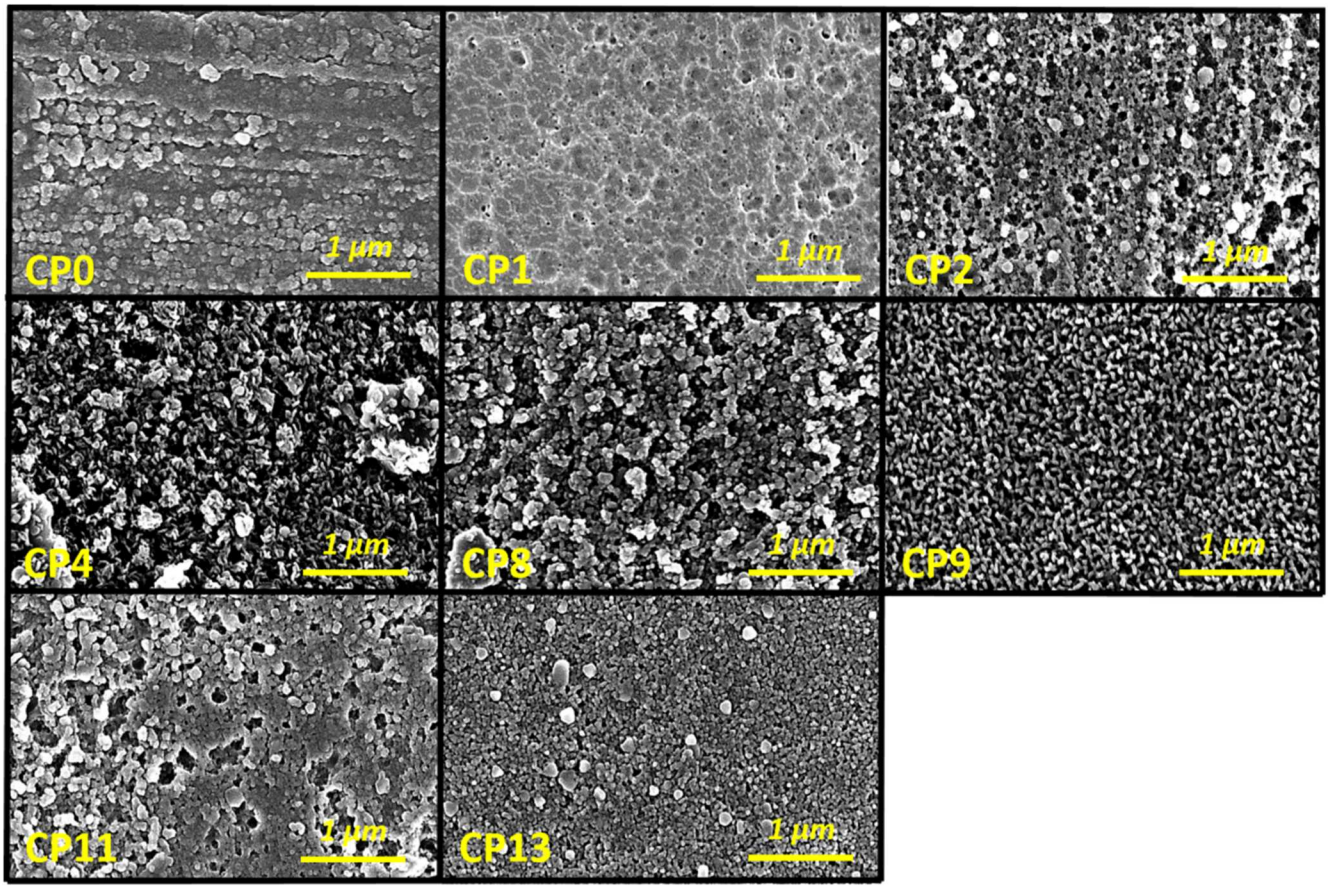

Figure 5. SEM-SE images (30000 × magnification) of AA7075 samples after different chemical pretreatments (Table I).

SE-SEM images at higher magnification (Fig. 5) show that commercial CP1 produced the most compact and uniform surface morphology with the smallest nanometric globules with clearly visible grain boundaries. CP9 also produced a uniform surface, but was composed of even larger globules, and grain boundaries were visible at the surface of AA7075. The rest of the CPs produced similar surface morphology, consisting of larger globules and pores between them.

EDS analysis showed that all CPs except CP9 removed a spontaneously formed Al oxide from the surface and significantly reduced the surface Mg content (Table II). The thickness of the aluminium oxide layer after CPs can be determined by measuring the surface concentration of Al and O. A higher content of Al and a lower content of O means that the thickness of aluminium oxide is smaller, and vice versa. Commercial CP1 produced the thinnest layer of Al oxide, reduced the content of Mg and somewhat increased the concentration of Cu and Zn at the surface compared to CP0. After CP1, 1 at% of F was detected at the surface. After CP13, the thickness of Al oxide was also reduced, but it was around 3-fold thicker than that after CP1; the concentration of Mg was reduced, and that of Cu and Zn was increased compared to CP0. F was also detected at the surface. However, the comparison between CP1 and CP13 shows that the Zn concentration was slightly higher in CP1, 3.7 at% vs 2.5 at%. After CP9, which is the modification of CP1 with an additional formation of pseudoboehmite, the O concentration increased from 6 at% to 62 at%. The Mg, Cu, and Zn concentrations were smaller, and that of F remained at the same level as CP1. This result confirmed the formation of a thick pseudoboehmite layer that covered the surface of AA7075. The surface morphology followed the pattern of CP1 morphology.

From the rest of the CPs, it is important to notice that CP8, consisting of alkaline etching based on the combination of NaOH and H_3PO_4, decreased the content of Mg at the surface (1.8 at%) but significantly increased the content of Zn up to 13.7 at% and Cu up to 5.7 at% compared to bare AA7075 (CP0). P was detected at the surface in a concentration of 1.1 at%. CP4 with strong alkaline etching resulted in enrichment in Cu and Zn at the surface with concentrations of 3.0 and 6.8 at%, respectively, compared to bare AA7075 (CP0).

To summarise, the thickness of aluminium oxide layers after CPs was in the following order from lowest to highest: CP1 $<<$ CP13 $\approx$ CP2 $<$ CP11 $<$ CP8 $<$ CP4 $<$ CP0 $<<$ CP9. All pretreatments significantly reduced the surface Mg content relative to CP0, except for the strong alkaline etching pretreatment of CP4, which left 4.7 at % of Mg at the surface. Alkaline etching of CP4, which consisted of NaOH, caused the enrichment of Cu and Zn at the surface. Alkaline etching of CP8, which consisted of NaOH and H_3PO_4, decreased the content of Mg at the surface but increased the content of Zn to 13.7 at% and Cu to 5.7 at%. The commercial CP1 produced the thinnest aluminium oxide layer, exposed grain boundaries, reduced Mg content and slightly increased the surface contents of Cu, Zn and F compared to CP0.

SEM-EDS characterisation of zirconium conversion coatings applied on AA7075.—SEM SE, and BSE images of ZrCC-coated AA7075 samples after various chemical pretreatments are presented in Figs. 6, 7 and S8. The corresponding average compositions obtained by EDS analyses are given in Table II. SE (Fig. 6) and BSE (Fig. S8) SEM images show that ZrCCs follow the surface morphology of chemically pretreated surfaces. CP1-ZrCC applied after commercial SurTec® CP had the most uniform and compact surface morphology. The grain boundaries remained clearly visible, indicating that the conversion coating followed the surface pattern and was not thick enough to mask them. The same trend was noticed for all other surface pretreatments.

EDS analysis (Table II) showed that after the conversion coating process, Zr and F were detected at the surface of all samples, with

Table II. EDS analysis of chemically pretreated AA7075 and ZrCC-coated AA7075 samples. The electron beam voltage was 3 kV, corresponding to an analysis depth of ca. 100 nm. *CP1-A-ZrCC represent EDS analysis of the sample without pitting after 15 days of immersion in 0.1 M NaCl solution. **CP1-B-ZrCC represents the EDS analysis of the pit area of the sample pitted after 15 days of immersion in 0.1 M NaCl solution. For quantification, please refer to the footnote.[a)]

Treatment	Composition/at%							
	Al	O	Zr	F	Mg	Cu	Zn	P
CP								
CP0	42	33			21.9	1.0	2.1	
CP1	87	6		1	2.2	1.7	2.5	
CP2	75	17			1.6	2.4	3.7	
CP4	58	27		<1	4.7	3.0	6.8	
CP8	54	23			1.8	5.7	13.7	1.1
CP9	36	62		1	0.3	0.4	0.3	
CP11	73	20		<1	1.7	1.5	3.5	
CP13	74	18		<1	1.9	1.8	3.7	
ZrCC								
CP0-ZrCC	33	34	14.0	6	10.8	0.8	1.5	
CP1-ZrCC	46	29	13.8	7	1.3	1.4	1.7	
CP2-ZrCC	38	40	11.2	6	1.3	1.8	2.2	
CP4-ZrCC	41	40	1.3	4	3.8	2.7	7.2	
CP8-ZrCC	23	52	8.0	5	0.9	5.3	4.4	1.3
CP9-ZrCC	24	63	5.8	6		0.7	0.5	
CP11-ZrCC	32	46	9.9	8	0.7	1.0	2.1	
CP13-ZrCC	36	41	10.5	10	0.9	0.7	1.4	
ZrCC-15d								
CP1-A*-ZrCC	46	36	11.9	2	1.1	1.7	2.0	
CP1-B**-ZrCC	33	62	2.3	2	<0.5	<0.5	<0.5	

a) In EDS, detection limits are typically considered to be ⩾1% for low atomic number elements (Be to F) and ⩾0.1% (1000 ppm) for higher atomic number elements. With standardless quantitative EDS, which is most often used, relative errors may be ±2% to ±5% for major components (https://www.jeolusa.com). Accordingly, in the tables, concentrations for light elements (O and F) were rounded to 1 at%, as well as for Al as a major element coming from the substrate.

concentrations from 5.8 to 14.0 at% and from 4 to 10 at%, respectively, indicating the formation of conversion coatings. The only exception was sample CP4, with a Zr concentration of only 1.3 at%; in that case, ZrCC was not formed or, more likely, formed on top of a thick, cracked aluminium/magnesium oxide-hydroxide layer.

The surface concentrations of Zr and F of CP1-ZrCC were 13.8 at% and 7 at%. The O concentration increased to 29 at% compared with 6 at% for bare CP1, indicating that 22 at% of O was associated with CP1-ZrCC. Al, Mg, Cu and Zn were also detected at the surface, but at lower concentrations due to the presence of the conversion coating. Compared to CP1-ZrCC, sample CP0-ZrCC had a similar Zr content (14.0 at%), a lower F content (6 at%) and a significantly higher Mg content (10.8 at%), indicating that Mg was present in CP0-ZrCC.

CP13-ZrCC had 10.5 at% Zr and 10 at% F, and the O content in ZrCC was around 23 at%. CP9-ZrCC had 5.8 at% and 6 at% Zr and F, and 63 at% O, indicating that conversion coating was formed at the top of the pseudoboehmite layer.

Analysis of EDS data in Table II shows that the best corrosion protection (as presented in Figs. 1 and 2) was achieved with CP1-ZrCC, with an optimal Zr/F ratio of around two and the surface Zr concentration of 14.0 at%. SEM analysis showed that the coating is compact and uniform, with a nanometric globular structure (Figs. 7 and S8).

XPS characterisation of chemically pretreated bare and ZrCC-coated AA7075.—CP AA7075 samples and ZrCC-coated AA7075 samples were characterised with XPS. The XPS method, with an analysis depth of *ca.* 10 nm, provides information from the topmost surface of the samples. The composition of the surface obtained from the XPS survey spectra is presented in Table III. In general, after CPs, the concentration of Al and O increased in all samples compared to the bare CP0 sample, indicating that aluminium hydrated oxide and oxides of minor components were formed during chemical cleaning. This increase was significantly higher for alkaline CP2, CP4, CP8 and pseudoboehmite pretreatment CP9, indicating the formation of thicker oxide layers. After strong alkaline pretreatment (CP4) and phosphate alkaline pretreatment (CP8), the concentrations of Mg, Cu and Zn at the surface increased compared to bare AA7075 (CP0), whereas in all other CPs, Mg was removed. After commercial CP1, the Mg concentration decreased from 11.1 at% to 0.2 at%. F, Si, Cu, Zn, N, and S were detected at the surface in concentrations of 2.4 at%, 1.0 at%, 0.4 at%, 0.1 at%, 0.5 at%, and 1.0 at%, respectively. F, Si and S were detected only in CP1, which showed superior corrosion protection after ZrCC application. Further, Mg was almost completely removed from the surface. After CP13, which used concentrated HNO_3 desmutter instead of commercial SurTec 496®, there was no F, Si, Mg and Cu at the surface; instead, N and Zn were detected.

After CP9, which differs from CP1 only by the additional step of pseudoboehmite formation, the O concentration increased from 42 at % to 62, confirming that a pseudoboehmite layer of aluminium oxide was formed after immersion in boiling Di-H_2O. The Cu concentration was below 0.5 at%.

After applying ZrCCs, Zr and F were detected at the surface with concentrations of 4.2–11.0 at% and 2.3–5.5 at%, respectively. The lowest Zr and F contents and the highest Mg content were detected in the CP4-ZrCC. Also, in the CP8-ZrCC sample subjected to CP8 phosphate-alkaline pretreatment, low concentrations of zirconium (6.8 at%) and fluorine (3.4 at%) were detected, alongside elevated levels of magnesium and zinc. A minor presence of copper was also observed.

For CP0-ZrCC, a small content of Mg and Zn was detected at the surface, suggesting that these two elements were present at the top layer of the conversion coating. For CP1-ZrCC, the concentrations of Zr and F were 8.6 at% and 2.4 at%, respectively, giving a Zr/F ratio of 3.6. A minor content of Cu and Zn was detected at the surface of CP1-ZrCC, indicating that Cu and Zn were part of the top layer of ZrCC. CP13-ZrCC had 5.5 at% of F and 10 at% of Zr, giving a ratio Zr/F of 1.81, which is lower than that in the best-performing CP1-ZrCC. It should be noted that the CP1-ZrCC had the highest concentration of C contamination (53.3 at%) at the surface, which may be indicative of a stronger bonding tendency of the CP1-treated surface toward organic species.

High-energy resolution XPS spectra for the elements of interest are presented in Figs. 8 and 9. For most CPs, one broad Al 2p peak centred at the binding energy (E_b) between 74.2 eV and 74.7 eV corresponding to $Al(OH)_3$ was noted. For CP9, this peak had the highest intensity and was shifted to a lower E_b of 73.8 eV, indicating the formation of a thick pseudoboehmite layer. Only in the case of CP1 did two separated peaks appear at E_b of 72.5 eV and 74.7 eV (Fig. 8a), corresponding to Al metal and $Al(OH)_3$, respectively.[82,83] This means that after CP1, the thinnest Al oxide/hydroxide layer was formed, allowing Al metal to be detected at the surface.

After the formation of ZrCC (Fig. 9a), the intensity of the Al peaks decreased, and they were centred at 74.1–74.5 eV. The lowest intensity was observed for CP0-ZrCC and CP1-ZrCC, followed by CP2-ZrCC, CP11-ZrCC and CP13-ZrCC. For CP4-ZrCC, CP8-ZrCC and CP9-ZrCC, the Al 2p peak was higher, indicating that ZrCC was thinner and formed on top of the Al hydroxide/pseudobohemite layer or Al–Mg hydroxide in the case of CP8-ZrCC. Correlating these observations with SEM-EDS analysis indicates that for CP9-ZrCC and CP4-ZrCC, the conversion coating was deposited on the top of the Al hydrated oxide formed during the chemical pretreatments.

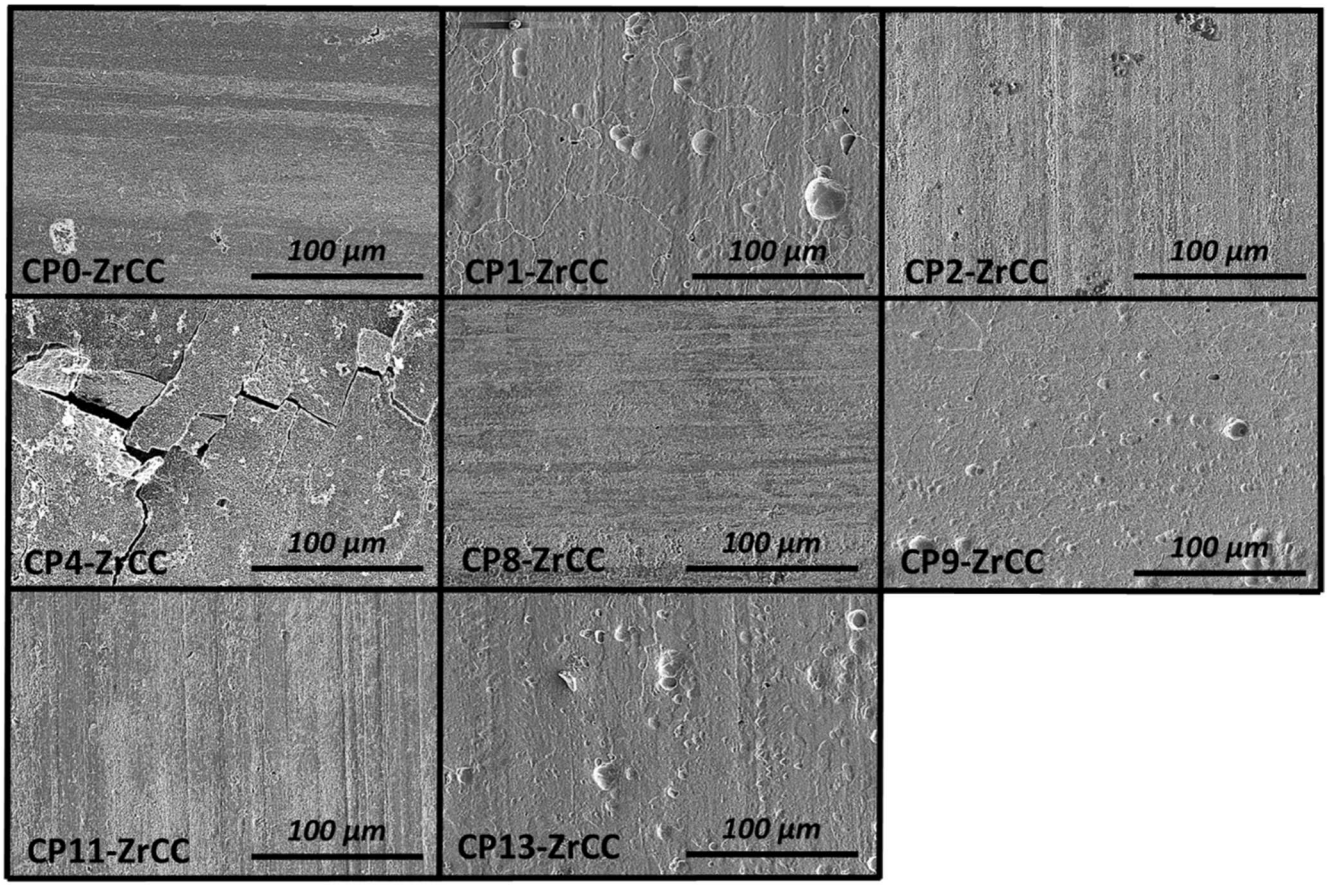

Figure 6. SEM-SE images (500 × magnification) of ZrCC-coated AA7075 samples after different chemical pretreatments (Table I).

For all chemically pretreated AA7075 samples, the O 1s peaks were centred at 531.2–532.0 eV, indicating the prevalence of hydroxide over oxide (Fig. 8b). For CP1, the peak was centred at 532 eV, indicating the highest concentration of Al hydroxide compared to other samples. Qualitatively, three peaks could be identified—for bound H_2O, $Al(OH)_3$ and $ZrO_2{\cdot}xH_2O$, at 533 eV, 532 (531.9) eV and 530.5 eV, respectively.[83,84] In the case of phosphate-alkaline pretreatment CP8, the O 1s peak exhibited the highest intensity and was centred at 531.9 eV, attributable to the formation of an increased content of magnesium hydroxide and, potentially, zinc hydroxide species. After the conversion coating process, the centre of the O 1s peak shifted to 531.1–531.6 eV, depending on pretreatment, and showed a shoulder at 530.5 eV that corresponds to hydrated Zr oxide and oxyfluoride ($ZrO_2{\cdot}xH_2O/ZrO_xF_y$) (Fig. 9b).

The F 1s peak was centred at E_b 687.0 eV and was present only after commercially pretreatment CP1, suggesting the presence of AlO_xF_y (Fig. 8d). After the ZrCC process, the F 1s peak appeared for all samples, and it was centred at E_b from 684.5 eV to 685.0 eV, related to ZrF_4/ZrO_xF_y in the top layer (Fig. 9d).

After the conversion coating process, Zr was detected at the surface (Fig. 9c). The Zr $3d_{5/2}$ and $3d_{3/2}$ peaks for the as-prepared conversion coatings were centred at 184.1–185.0 eV and 182.0–182.7 eV, respectively, depending on surface pretreatment. These spectra relate to a mixture of ZrF_4/ZrO_xF_y and $ZrO_2{\cdot}xH_2O$ since the coating contained a relatively high fluorine and oxygen concentration (Table III).[85] A higher shift to lower E_b indicates the prevalence of $ZrO_2{\cdot}xH_2O$ over ZrF_4/ZrO_xF_y in the top layer of the conversion coating.

The Cu 2p peak was detected for chemical pretreatments CP1, CP2, CP4, CP8, CP9 and CP11 (Fig. 8c). Its Cu $2p_{3/2}$ peak was centred at 933.2 eV in the case of CP1, CP2 and CP11, while for CP9 and CP4 it was at 932.8 eV and 932.5 eV, respectively. This observation suggests the presence of Cu compounds on the surface following these pretreatment processes. (Fig. 9g). Copper was present either as metal or Cu(I) because no satellite peak characteristic of Cu(II) species appeared above the main peak (results not shown).

The Zn $2p_{3/2}$ peaks were centred at 1021.7 eV and 1022.2 eV after CP2, CP4 and CP8, indicating the presence of Zn compounds at the surface after these two surface pretreatments (Fig. 8f). Peak intensity was stronger for CP8 and CP4 than for CP2, indicating that phosphate-alkaline pretreatment and strong alkaline pretreatment produced more enrichment of Zn at the surface. After the conversion coating process, the Zn 2p peak was present only for CP4-ZrCC (Fig. 9f).

The Mg 1s peak was detected for the CP0, CP4 and CP8 samples. It was centred at 1003.5 eV and 1003.7, respectively (Fig. 8e). The peak intensity was stronger for CP8 and CP4 than for the CP0 sample, indicating enrichment of Mg at the surface after phosphate-alkaline pretreatment and strong alkaline pretreatment of CP4. After the conversion coating process, the Mg 1s peak was present for CP4-ZrCC and CP8-ZrCC (Fig. 9e).

ToF-SIMS characterisation of chemically pretreated bare and ZrCC-coated AA7075.—ToF-SIMS was employed to investigate the structure, thickness and composition of aluminium oxides after surface pretreatments and to assess their influence on the structure, composition and thickness of subsequently deposited ZrCCs. The ToF-SIMS method provides meaningful information regarding these aspects. Although ToF-SIMS exhibits depth resolution comparable to that of XPS and Auger electron spectroscopy (AES), it offers a significantly faster profiling rate, which was one of the main reasons for its selection over depth-profiling using XPS, and, at the same time, for the distribution of interfacial species and compositional gradients.

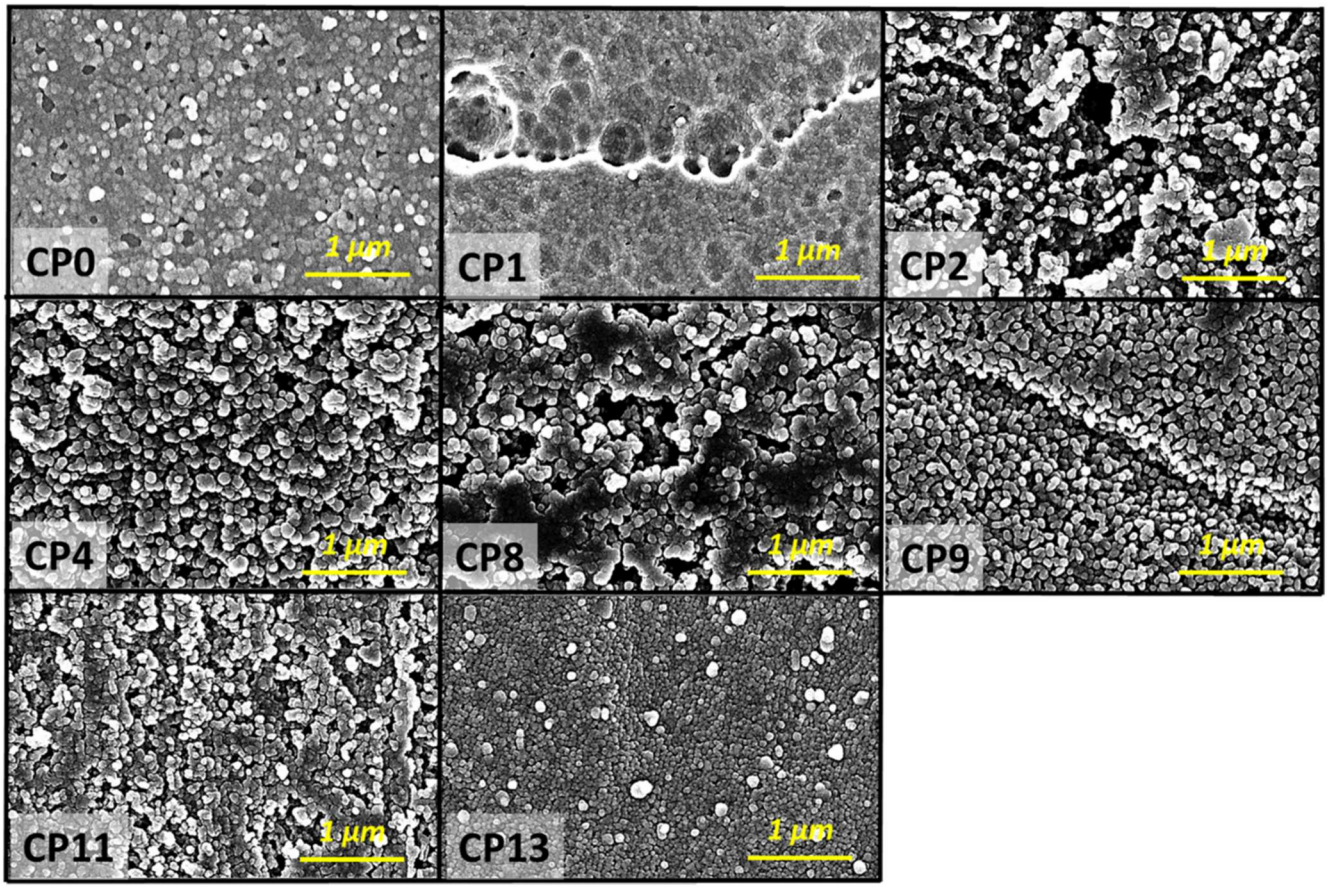

Figure 7. SEM-SE images (30000 × magnification) of ZrCC-coated AA7075 samples after different chemical pretreatments (Table I).

Table III. XPS analysis of chemically pretreated AA7075 and ZrCC-coated AA7075 samples. *CP1-A*-ZrCC- represents XPS results of the sample without pitting after 15 days of immersion in 0.1 M NaCl solution.

Treatment	Composition/at%											
	C	Al	O	Zr	F	Si	Mg	Cu	Zn	S	N	P
						CP						
CP0	42.8	5.1	36.6		0.5	1.4	11.1		0.3		1.3	0.9
CP1	28.7	23.2	42.5		2.4	1.0	0.2	0.4	0.1	1.0	0.5	
CP2	27.0	19.8	48.1				0.3	1.9	1.1		0.4	1.4
CP4	17.1	8.6	53.6				16.2	0.9	3.6			
CP8	7.1	8.1	58.3		0.2		19.5	0.4	4.0			2.4
CP9	15.7	22.1	61.9					0.3				
CP11	31.6	18.0	48.7					0.3			0.7	0.7
CP13	38.3	15.3	44.8						0.4		1.2	
						ZrCC						
CP0-ZrCC	41.9	0.7	42.0	11.0	3.0		1.2		0.2			
CP1-ZrCC	53.3	2.2	33.1	8.6	2.4			0.2	0.2			
CP2-ZrCC	43.7	6.5	37.1	9.0	2.3			1.3	0.1			
CP4-ZrCC	17.5	9.1	48.5	4.2	2.6		11.5	2.0	4.6			
CP8-ZrCC	40.6	4.4	37.1	6.8	3.4		5.8	0.4	1.5			
CP9-ZrCC	31.5	8.4	48.2	8.6	2.9			0.4				
CP11-ZrCC	40.6	4.4	41.9	9.7	3.3			0.1				
CP13-ZrCC	37.1	4.2	43.0	10.0	5.5			0.2				
						ZrCC-15d						
CP1-A-ZrCC	44.5	2.3	43.7	8.0	0.5						1.0	

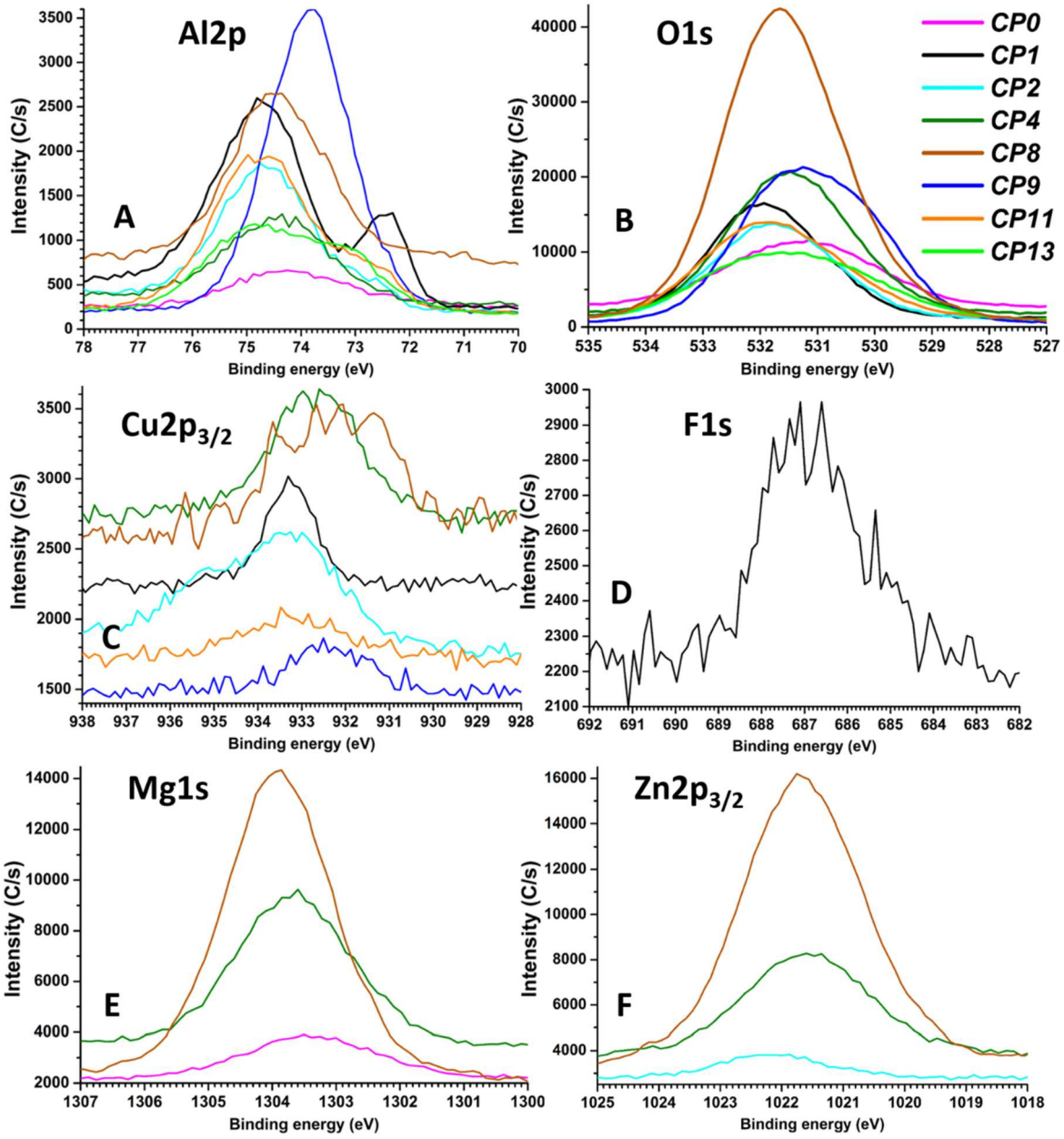

Figure 8. High energy resolution XPS spectra (a) Al 2p, (b) O 1s, (c) Cu 2p, (d) F 1s, (e) Mg 1s and (f) Zn $2p_{3/2}$ for chemically pretreated AA7075 (Table I). Spectra were not normalised on the intensity scale.

ToF-SIMS negative-ion profiles were recorded and presented for selected ion fragments: MgO^-, $AlOF^-$, CuO^-, ZnO^-, SiO^-, FeO^-, S^-, AlO^-, Al_2^-, PO_3^- and F^- (Figs. 10–13).

The thicknesses of Al-hydrated oxide and ZrCCs determined from ToF-SIMS ion depth profiles are given in Fig. 14 and Table IV and SIV. The thickness of aluminium oxide after surface pretreatments was determined as the point at which the intensity of AlO^- dropped to a half its maximum value (Figs. 11–13). The boundary between the outer and inner layers of ZrCCs was determined as the point at which the intensity of ZrO^- dropped to half its maximum value. The point at which the $AlOF^-$ intensity dropped to half its maximum value was taken as marking the boundary between the inner layer and substrate (denoted by Al_2^-).

After CP0, the thickness of the Al hydrated oxide (determined from the AlO^- profile) was 120 nm. Surface pretreatments reduced the thickness of Al-hydrated oxide after CP1, CP2, CP11 and CP13. In contrast, the thickness of Al/Mg hydrated oxides was increased after CP4, CP8 and CP9 (Fig. 14a). After CP1, the thinnest layer of Al oxide of around 10 nm and very thin layers (6 nm) of Al oxyfluoride and sulphur were determined. For other pretreatments, Al oxyfluoride and sulfur were not detected (Figs. 10, 11 and 14).

Negative-ion profiles showed that the bare sample CP0 had a layer of Mg hydrated oxide at the surface (Fig. 10). This layer was even thicker after strong alkaline pretreatment CP4, and it was followed by layers of CuO^- and ZnO^- ion fragments of the same intensity. FeO^- and SiO^- negative-ion profiles of lower intensity were also noted. This finding means that CP4, as an intense alkaline CP, strongly enriches the surface in Mg, Cu, Zn, Si and Fe ions. Following phosphate-alkaline pretreatment of the CP8 sample, the surface layer exhibited significant enrichment in MgO^- and PO_3^- ion fragments. Additional species, including FeO^-, CuO^-, SiO^-, and ZnO^-, were also detected, displaying depth profiles that closely paralleled those of PO_3^-. Notably, SiO^- was present within the top layer but exhibited a depth distribution shifted toward the substrate, mirroring the profile of AlO^-. These observations suggest that the phosphate-alkaline treatment facilitated the incorporation of

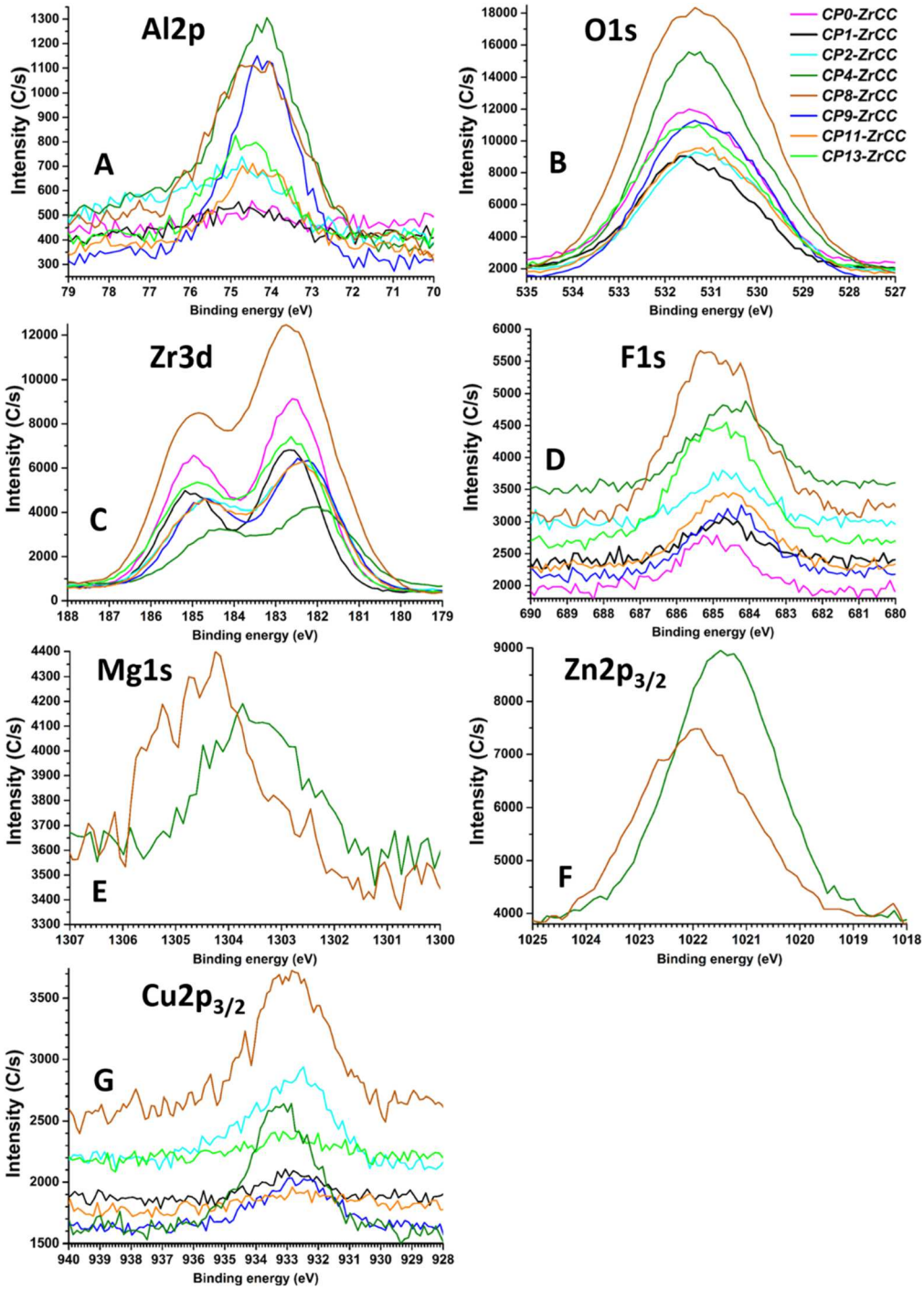

Figure 9. High energy resolution XPS spectra (a) Al 2p, (b) O 1s, (c) Zr 3 d, (d) F 1s, (e) Mg 1s, (f) Zn $2p_{3/2}$ and (g) Cu $2p_{3/2}$ for ZrCC-coated AA7075 samples after various chemical pretreatments (Table I). Spectra were not normalised on the intensity scale.

hydrated metal oxides and phosphate species—particularly of Fe, Cu, Zn, and Mg—into the top surface region. The shifted profiles of AlO^- and SiO^- indicate the presence of an underlying layer enriched in aluminium hydroxide and silicon oxide species.

Recorded negative-ion profiles showed that CP2, CP4, CP8, CP11 and CP13 also enriched the surface with Cu, Zn, Si, and Fe. Commercial pretreatment CP1 has the surface enriched in Al oxyfluoride ($AlOF^-$), sulfur (S^-), fluoride (F^-), and copper (CuO^-) and depleted in Mg (MgO^-). This enrichment was concentrated in a very thin layer at the surface of AA7075 and followed the AlO^- pattern (Fig. 11), indicating very uniform and compact layers of these elements and their oxides at the surface. These are the main differences between CP1 and other CPs. Surface pretreatment CP9 with the additional step of pseudoboehmite formation, compared to CP1, produced the thickest layer of aluminium oxide (Fig. 11) of at least 300 nm and redistributed surface elements (Fig. 10) through the newly formed layer of thick Al hydrated oxide.

After the conversion coating process, the ZrO^- ion profile appeared, indicating the formation of ZrCC (Fig. 12). The $AlOF^-$ profiles intensified for all samples. All CPs except CP9 showed a bilayer structure of ZrCC. According to negative-ion profiles, for CP9-ZrCC, ZrO^- and F^- ion fragments were present throughout the depth profile (Figs. 12 and 13), indicating the formation of ZrCC on top and within the pseudoboehmite layer. Fluoride ions penetrated even deeper inside this layer and formed Al oxyfluorides.

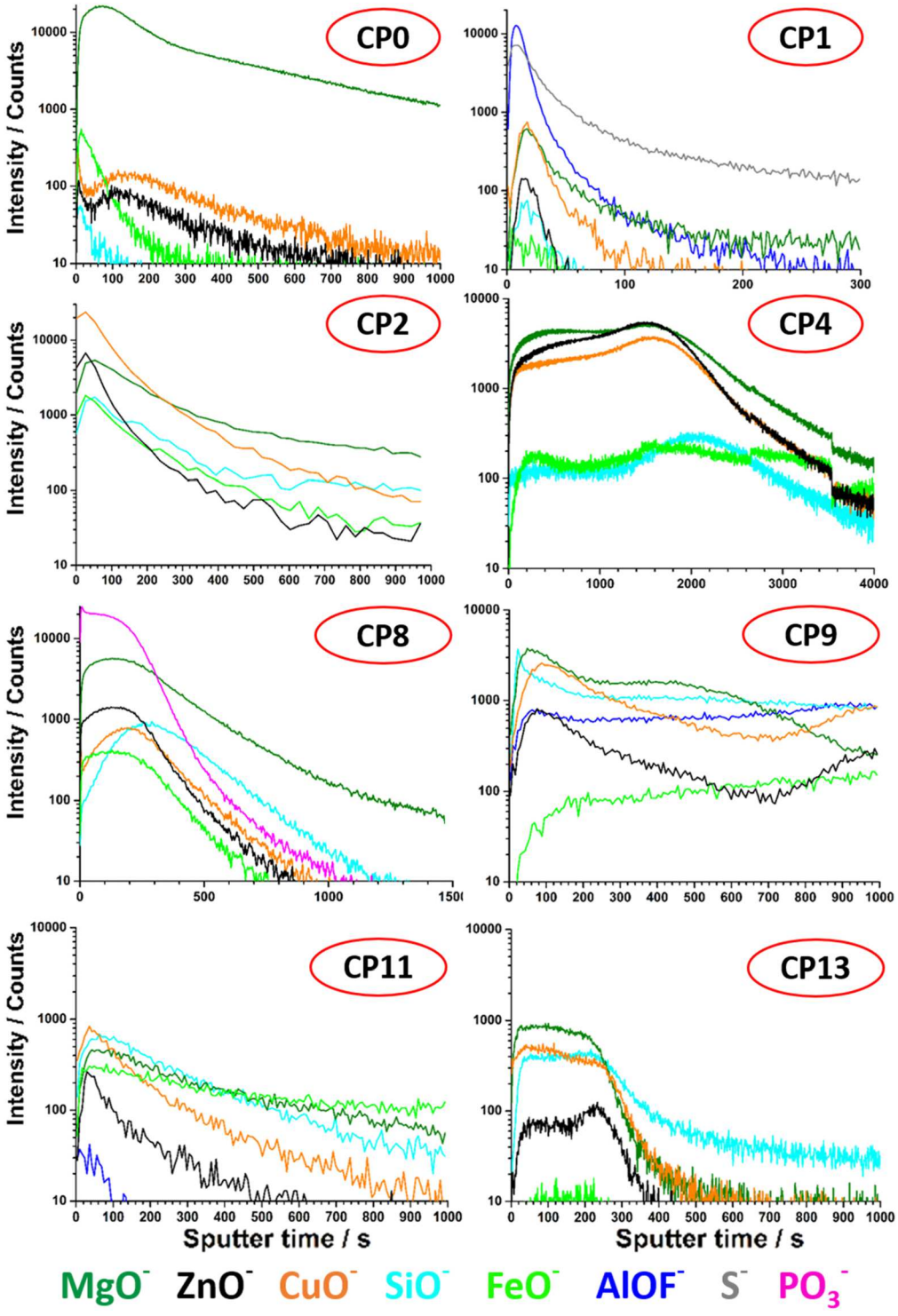

Figure 10. ToF-SIMS negative-ion depth profiles of chemically pretreated AA7075 samples (Table I). Sputtering rate was 0.3 nm s^{-1}.

Negative-ion depth profiling of the CP8-ZrCC system revealed a distinct bilayer architecture induced by phosphate-alkaline pretreatment (CP8). The outermost layer was markedly enriched in MgO^- and PO_3^- ion fragments, both of which exhibited consistent ion profiles throughout the coating thickness. Additional signals corresponding to ZrO^-, $AlOF^-$, FeO^-, CuO^-, SiO^-, and ZnO^- were also detected, albeit at significantly lower intensities, yet following a similar depth distribution. The underlying (inner) region was predominantly composed of ZrO^- and $AlOF^-$ species, accompanied by FeO^-, CuO^-, SiO^-, and ZnO^- ions exhibiting overlapping trends. Notably, the depth profiles of AlO^- and F^- mirrored those of ZrO^- and $AlOF^-$, further confirming the stratified nature of the coating. These findings strongly indicate that incorporating phosphate species during CP8 pretreatment modulates the growth mechanism of the ZrCC layer, leading to a chemically heterogeneous bilayer structure. Specifically, the upper layer is characterised by the presence of magnesium hydroxide and phosphate-rich phases, whereas the inner layer is dominated by zirconium oxide and aluminium oxyfluoride species, with trace contributions from Fe-, Zn-, Cu-, and Si-containing oxides.

Table IV. The thickness of aluminium oxide (determined from AlO^- ion fragment profile, Fig. 11) and ZrCC applied on AA7075 after different chemical pretreatments (Table I). The thickness of zirconium conversion coatings was determined as the depth at which the intensity of $AlOF^-$ negative ions dropped to a half value of its maximum value (Fig. 12). Sputtering rate was 0.3 nm s^{-1}. *Negative-ion profiles for CP4-ZrCC could not be recorded due to heavy charging of the sample, which caused damage to the coating.

Sample	Thickness, nm
CP0	120
CP0-ZrCC	78
CP1	12
CP1-ZrCC	42
CP2	54
CP2-ZrCC	78
CP4	145
CP4-ZrCC*	/
CP8	186
CP8-ZrCC	255
CP9	300
CP9-ZrCC	300
CP11	60
CP11-ZrCC	78
CP13	102
CP13-ZrCC	48

Negative-ion profiles of CP0-ZrCC differ from other ZrCCs by the presence of MgO^- and SiO^- ion fragments at the boundary between ZrCC and substrate, indicating that they were incorporated in the coating structure (Figs. 12 and 13). The comparison of the best-performing CP1-ZrCC to other CP-ZrCCs shows that it had S^- ions at the surface, which followed the ZrO^- profile. Among other ions with an intensity below 100 ppm, SiO^- followed the trend of ZrO^-, while CuO^- followed the $AlOF^-$ trend, indicating the incorporation of trace contents of Si in the top layer. CuO^- ion fragments were present in the lower parts of the ZrCC and at the coating/substrate interface.

The thickness of ZrCC ranged between 42 nm and 300 nm in the following order: CP1-ZrCC < CP13-ZrCC < CP0-ZrCC ≈ CP2-ZrCC ≈ CP11-ZrCC << CP8-ZrCC < CP9-ZrCC (Fig. 14b and Tables IV and SIV).

Looking only at ToF-SIMS profiles, the best corrosion protection and self-sealing performance of ZrCC-CP1 does not correlate well with its thickness. It would be expected that a thicker coating would provide better corrosion protection. However, this hypothesis was not confirmed because the thinnest CP1-ZrCC (42 nm) showed the best self-sealing ability and the most compact, uniform coating (Figs. 1–3 and 6). It appears that incorporating sulfur into the top layer of ZrCC improved the corrosion performance of CP1-ZrCC.

SEM-EDS analysis of CP1-ZrCC after 15 days of immersion in 0.1 M NaCl solution.—The samples were characterised after 15 days of immersion in 0.1 M NaCl solution to gain insight into the excellent corrosion performance and self-sealing mechanism of CP1-ZrCC. SE and BSE SEM on images of as-prepared CP1-ZrCC and CP1-ZrCC-15d are presented in Figs. 15 and 16. The corresponding EDS average analyses of ZrCC-coated samples are given in Table II. One CP1-ZrCC sample (CP1-B**-ZrCC) had a single pit after 15 days of immersion in 0.1 M NaCl (Fig. 16), while the other two samples of CP1-ZrCC (CP1-A*-ZrCC) were not pitted after 15 days of immersion (Fig. 15). Non-pitted CP1-ZrCC was more densified, and pores were almost completely closed in comparison with as-prepared CP1-ZrCC (Fig. 15, compare upper and lower rows). The SEM-BSE image of CP1-ZrCC with a single pit is presented in Fig. 16. The pit covered an area of $7.85 \cdot 10^{-5}$ cm^2, 0.006% of the total exposed area.

EDS analysis of the non-pitted samples (CP1-A*-ZrCC) showed that after 15 days of immersion, the concentration of O increased by 7 at% (from 29 to 36 at%), the F concentration decreased by 5.2 at%, while the concentration of Al and Zr decreased only slightly, i.e., by 0.3 at% and 1.9 at% (Table II). The concentration of minor elements Cu and Zn increased somewhat, and that of Mg was about constant. The difference in concentration of minor elements could be due to the inhomogeneity of AA7075 and CP1-ZrCC. These findings agree with the self-sealing mechanism we reported in our previous works.[34,78] The self-sealing mechanism was based on leaching F^- ions from the coating during immersion in 0.1 M NaCl solution, transforming ZrO_xF_y into $ZrO_2{\cdot}xH_2O$ and incorporating aluminium hydroxide into the coating structure.

EDS analysis of pit area (CP1-B**-ZrCC) showed a decreased concentration of Zr from 13.8 at% to 2.3 at%, and increased O concentration from 29 at% to 62 at%. This finding indicates that CP1-ZrCC at the pit area was unstable and dissolved, resulting in the formation of Al hydroxide. At the pitting area, Mg, Cu and Zn were detected at minor concentrations below 0.5 at%, indicating that pitting occurred at IMPs containing these elements.

XPS analysis of CP1-ZrCC after 15 days of immersion in 0.1 M NaCl solution.—XPS analysis of as-prepared CP1-ZrCC and CP1-ZrCC after 15 days of immersion is presented in Fig. 17 and Table III. XPS analysis was performed on the non-pitted sample (CP1-A*-ZrCC).

The concentration of F decreased from 2.4 at% to 0.5 at%, while the concentrations of Zr and Al remained constant. The O concentration changed from 33.1 at% to 43.7 at%; 1.0 at% of N was also detected. These results agree with the EDS analysis (Table II) and indicate that F is released from the CP1-ZrCC during immersion in 0.1 M NaCl and is replaced by OH, leading to the transformation of ZrO_xF_y into $ZrO_2{\cdot}xH_2O$ and to the incorporation of Al-hydrated oxide into the conversion coating.

High energy resolution XPS spectra of as-prepared CP1-ZrCC and CP1-ZrCC-15d for elements of interest are presented in Fig. 17. After 15 days of immersion, the intensity of the Al 2p peak increased, suggesting incorporation of Al hydroxide in the top layer of the coating. Its position was centred at the same E_b of 74.7 eV, corresponding to $Al(OH)_3$, as before immersion. The intensity of the O 1 s peak increased after 15 days of immersion. The peak shifted from 531.6 eV to 532 eV, indicating that the $Al(OH)_3$ content increased in the top layers. The F 1 s peak disappeared after 15 days of immersion, indicating F leaching from CP1-ZrCC. The Zr $3d_{5/2}$ and $3d_{3/2}$ peaks for CP1-ZrCC-15d had the same intensity as those for as-prepared ZrCC and were centred at 185.0 eV and 182.6 eV, respectively. The observed shift to lower binding energy for 0.1 eV may be related to the release of F and the transformation of ZrF_4/ZrO_xF_y into $ZrO_2{\cdot}xH_2O$.

ToF-SIMS analysis of CP1-ZrCC after 15 days of immersion in 0.1 M NaCl solution.—The ToF-SIMS technique was used to investigate the changes in the structure and composition of CP1-ZrCC after 15 days of immersion in 0.1 M NaCl solution (Fig. 18). The thicknesses of the outer and inner layers were determined as the points at which the AlO^- and ZrO^- ion profiles' intensity dropped to half their maximum value (Fig. 19). The values are shown in Table V.

The boundary between the outer and inner layers of ZrCCs was determined as the depth at which the intensity of ZrO^- dropped to half of its maximum value (Fig. 18). The depth at which the intensity of $AlOF^-$ dropped to half its maximum value was taken as marking the boundary between the inner layer and substrate.

Ion profiles of the as-prepared CP1-ZrCC and CP-ZrCC-15d show similar bilayer structures composed of zirconium oxide, predominantly concentrated in the top layer, and Al oxyfluoride in the inner layer. Al oxide was mainly present at the coating/substrate interface. Similar ion profiles and thicknesses indicate that the coating was not damaged after 15 days of immersion. The most

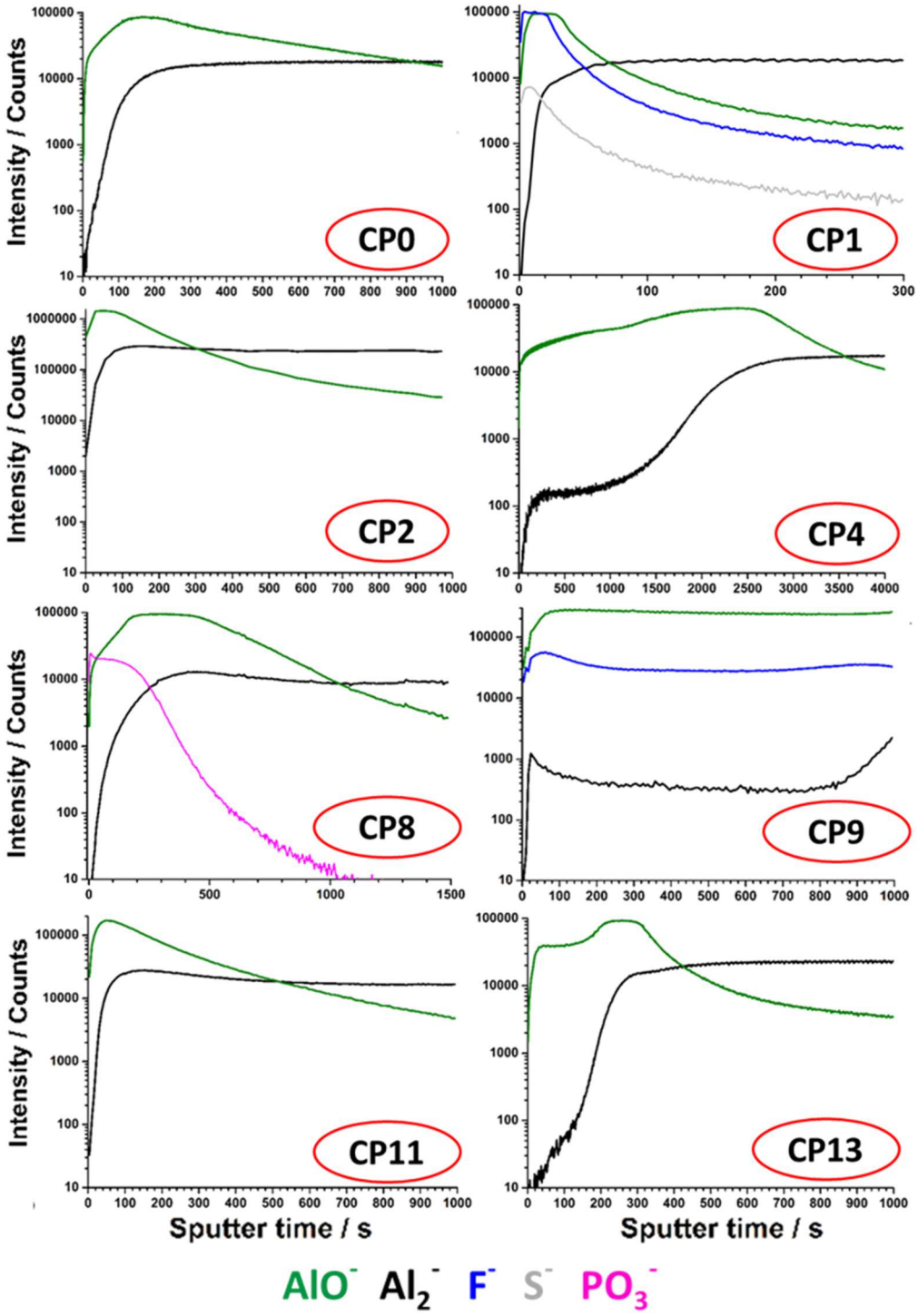

Figure 11. ToF-SIMS negative-ion depth profiles of chemically pretreated AA7075 samples (Table I). Sputtering rate was 0.3 nm s^{-1}.

interesting fact about CP1-ZrCC is that sulphur was part of the CP1-ZrCC and was concentrated predominantly in the top layer of CP1-ZrCC.

According to ion profiles, F^- leached out from the top layer of the coating, but it remained at the same level in the inner layer. The maximum in the sulphur ion profile was shifted towards the inner part, closer to the substrate, indicating the inward migration of these ions. Also, the maximum of AlO^- profile turned towards the substrate for about 10 nm, thus indicating the enrichment in Al hydrated oxides at the coating/substrate interface. Conversely, the SiO^- ion profile shifted from the inner layer of coating to the outer layer, reflecting the enrichment and possible incorporation of silicon oxide in the top layer of the CP1-ZrCC. Additionally, the intensity of Cl^- ion profiles increased 20-fold, indicating possible incorporation of Cl^- ions into the coating structure.

Discussion

This study underscores the pivotal role of chemical pretreatment in dictating the microstructural features and long-term corrosion resistance of Zr-based conversion coatings on 7075-T6 aluminium alloy. While prior studies have explored the effects of surface conditioning on coating formation, correlations with long-term electrochemical performance remain scarce.

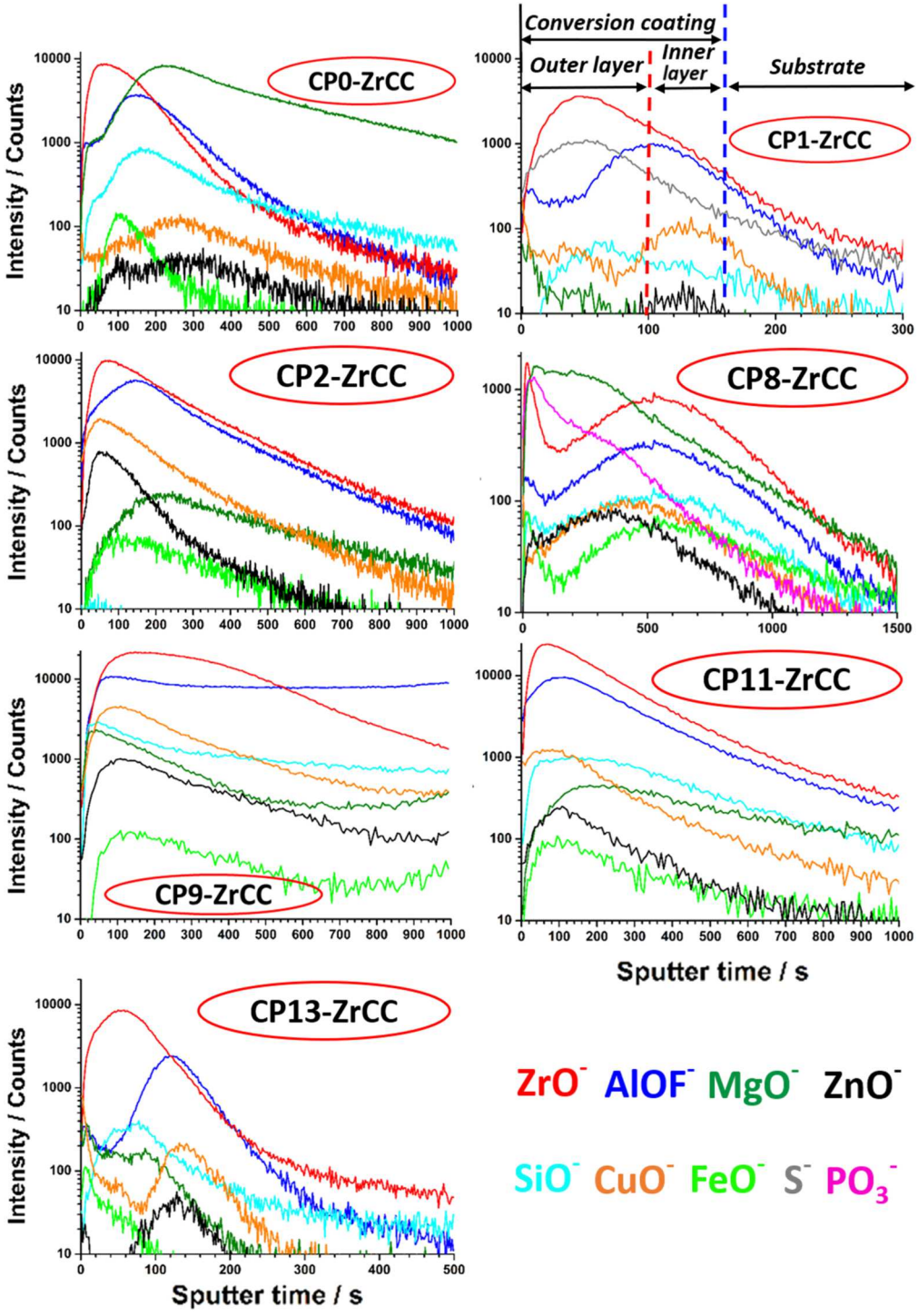

Figure 12. ToF-SIMS negative-ion depth profiles of ZrCC-coated AA7075 samples after various chemical pretreatments (Table I). Blue vertical dash line ─ the border between conversion coating and substrate; Red vertical dash line ─ the border between the outer and inner layers. Sputtering rate was 0.3 nm s^{-1}. The values of thicknesses are presented in Table IV.

Milošev and Rodič investigated the corrosion inhibition of AA7075-T6 using cerium acetate in chloride media and found that pretreatment with a slightly alkaline phosphate-based SurTec® cleaner followed by HNO_3 desmutting produced a highly protective surface.[65] This surface featured a dense, uniform layer enriched in cerium-acetate-derived oxides.[65] Similarly, Joshi et al. reported that alkaline activation significantly enhanced the deposition of cerium conversion coatings, yielding dense layers 300–500 nm thick, depending on treatment conditions.[68] Cerezo et al. systematically studied various pretreatment strategies—acidic, alkaline, thermal, and process-specific—for ZrCCs on aluminium alloys.[72–74] However, their work lacked electrochemical validation of corrosion protection, limiting the functional interpretation of microstructural findings. The effect of surface chemistry resulting from various chemical treatments was also verified on the hybrid sol–gel coatings deposited on Al, where the highest hydroxyl fractions obtained by pseudoboehmite treatment yielded the best adhesion of the top organic layer.[52]

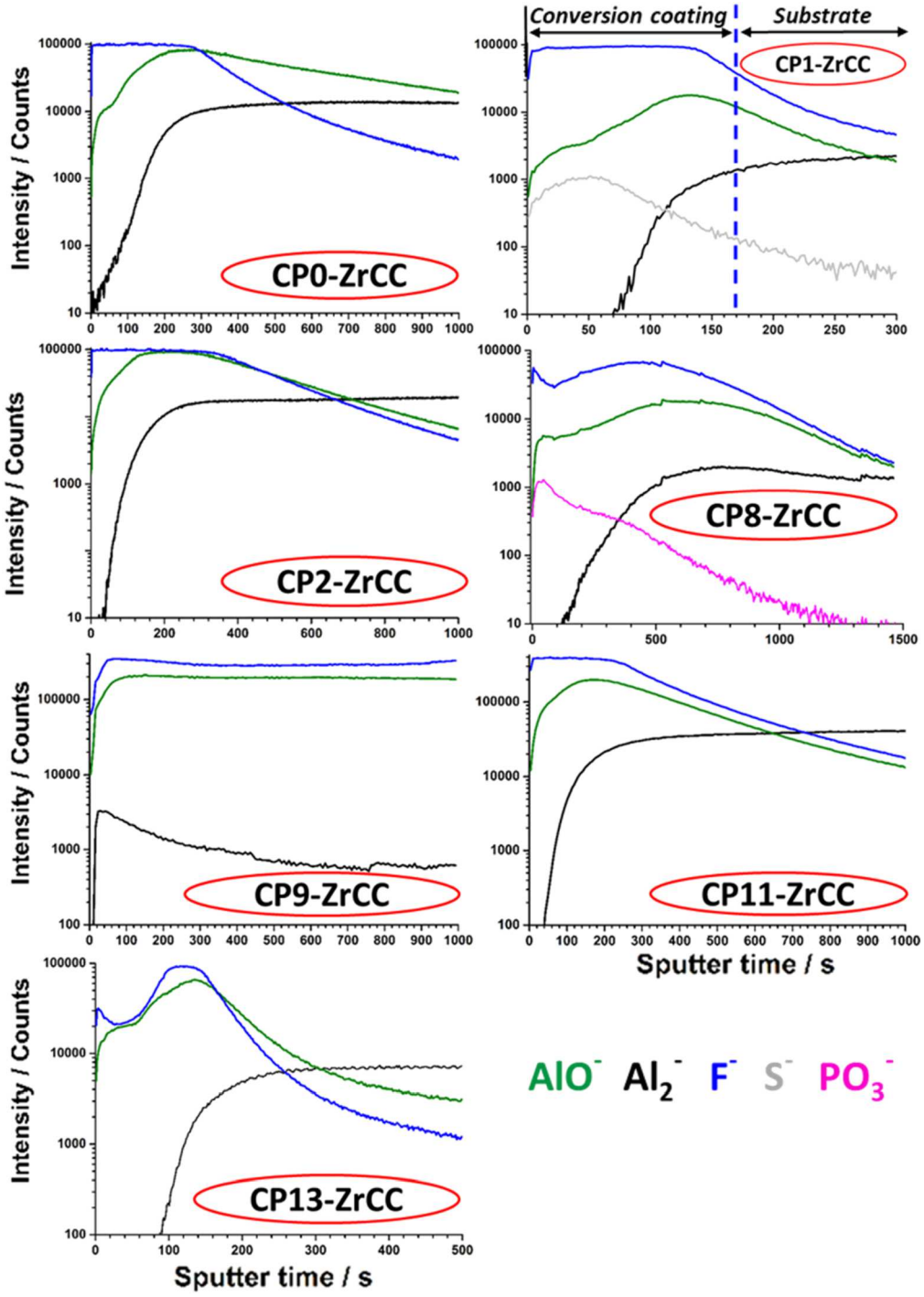

Figure 13. ToF-SIMS negative-ion depth profiles of ZrCC-coated AA7075 samples after various chemical pretreatments (Table I). Blue vertical dash line ─ the border between the conversion coating and substrate. Sputtering rate was 0.3 nm s^{-1}.

Our results highlight the need to correlate coating morphology and composition with electrochemical performance to assess the true protective efficacy of ZrCCs. Using EIS, immersion testing, and surface analysis, the commercial CP1 pretreatment—based on alkaline etching and proprietary desmutting—emerged as the most effective. CP1-ZrCC demonstrated a robust self-sealing effect during prolonged exposure in 0.1 M NaCl and achieved corrosion resistance comparable to that of the benchmark CP1-TCP system. Although CP1-TCP offered marginally better pitting resistance—likely due to the active inhibition by Cr(III) species—CP1-ZrCC showed superior performance among Zr-based systems.

Alternative pretreatments such as CP9 and CP13 offered moderate improvements over untreated CP0-ZrCC, with CP9 achieving higher impedance due to a more compact hydroxide layer. However, CP13—chemically similar to CP1 but employing HNO_3 for desmutting—performed markedly worse, highlighting the critical influence of desmutting chemistry on coating integrity. Other incomplete or non-optimised protocols led to significantly lower protection.

Polarisation studies indicated CP1-ZrCC acts mainly as a cathodic inhibitor, while CP1-TCP combines anodic and minor barrier inhibition. However, open circuit potential monitoring during prolonged immersion revealed that CP1-TCP maintained cathodic

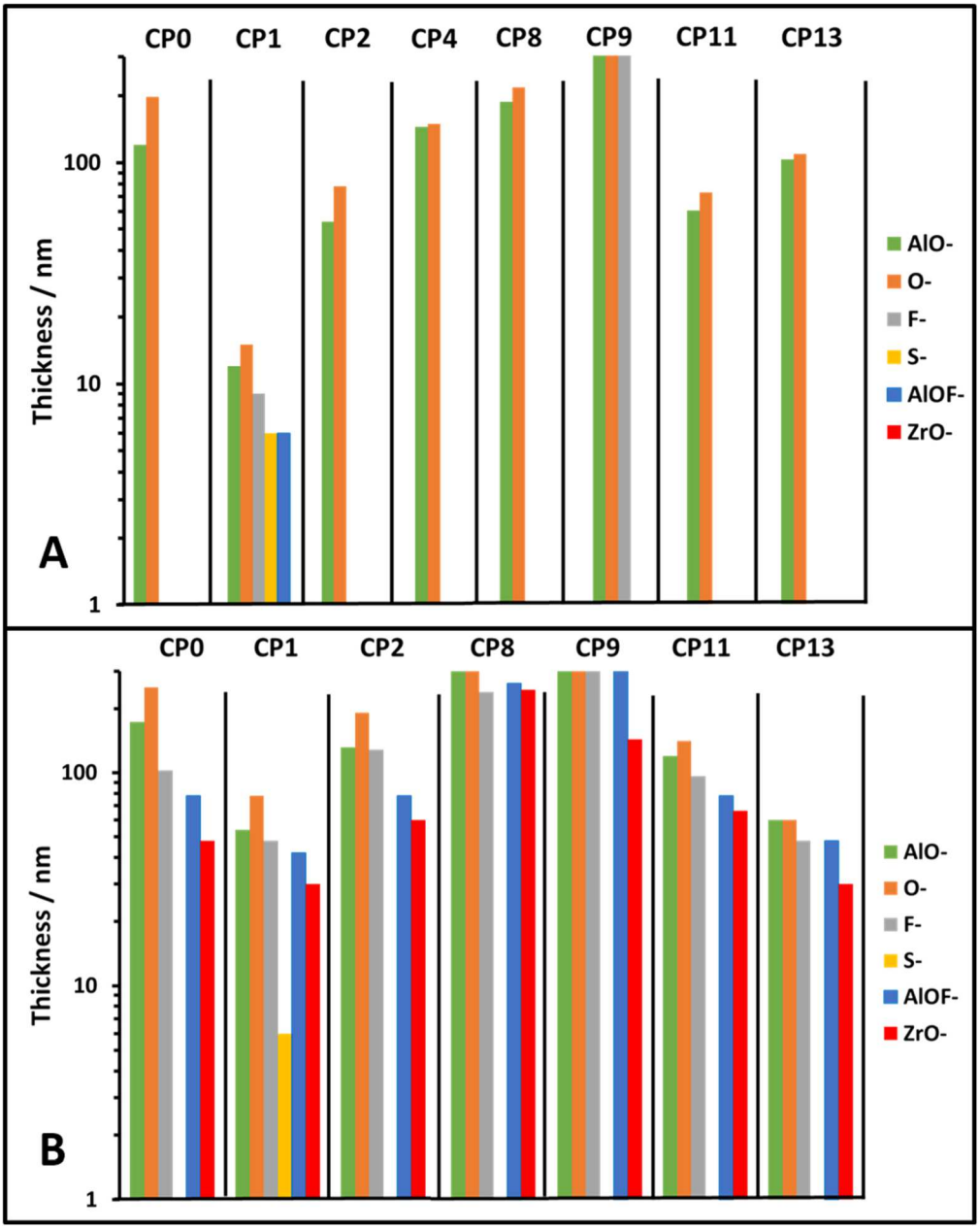

Figure 14. The thickness of negative-ion profiles for (a) chemically pretreated and (b) ZrCC-coated AA7075 samples. Chemical pretreatments are given in Table I.

inhibition throughout, whereas CP1-ZrCC, upon extended immersion, acted primarily as an anodic inhibitor with barrier properties.[22,23,34,41,58,78] This discrepancy underscores the need to combine electrochemical techniques to understand corrosion protection mechanisms fully.

Surface analysis showed that untreated CP0 featured an Al–Mg oxide layer. NaOH etching introduced surface enrichment with Cu, Zn, Si, and Mg, whereas acidic desmutting preferentially removed Mg and Zn. Boiling water post-treatment in CP1 generated a pseudoboehmite layer and enhanced elemental redistribution. CP8 pretreatment formed a thick, phosphate-containing Al–Mg oxide layer enriched with Zn, Fe, Cu, and Si, indicative of mixed oxide–phosphate species. In contrast, CP1 produced the most uniform Al oxide layer, incorporating minor F, S, and N, as well as redeposited Cu, Zn, and Si from intermetallic dissolution.

Post-deposition morphology was strongly dictated by pretreatment. Most ZrCCs exhibited a bilayer structure, with outer ZrO_2 and inner AlO_x/AlO_xF_y regions. Exceptions included CP9-ZrCC, which formed a porous monolayer due to the underlying pseudoboehmite, and CP8-ZrCC, where the coating integrated Mg, Zn, Cu, and Fe into the outer layer, deposited over a phosphate-rich hydroxide film. These findings highlight the complex interplay between pretreatment chemistry, substrate microstructure, and coating performance.

CP1-ZrCC, the best-performing coating, exhibited a ~40 nm bilayer structure comprising an outer ZrO_2-rich layer and an inner AlO_xF_y/aluminium oxide layer. ToF-SIMS identified S^- co-localised with ZrO^-, indicating sulfur incorporation from pretreatment. SiO^- and CuO^- ion fragments followed ZrO^- and $AlOF^-$ distributions, suggesting selective integration of Si near the surface and Cu at the interface. The coating retained the fine nanogranular morphology imparted by CP1, forming a dense and uniform layer. EDS showed 13.8 at% Zr with a uniform Zr/F ratio of 2, while XPS revealed a surface ratio of 3.6. This elevated Zr/F ratio correlated with enhanced barrier properties and self-sealing behaviour, affirming CP1-ZrCC's superior corrosion resistance.

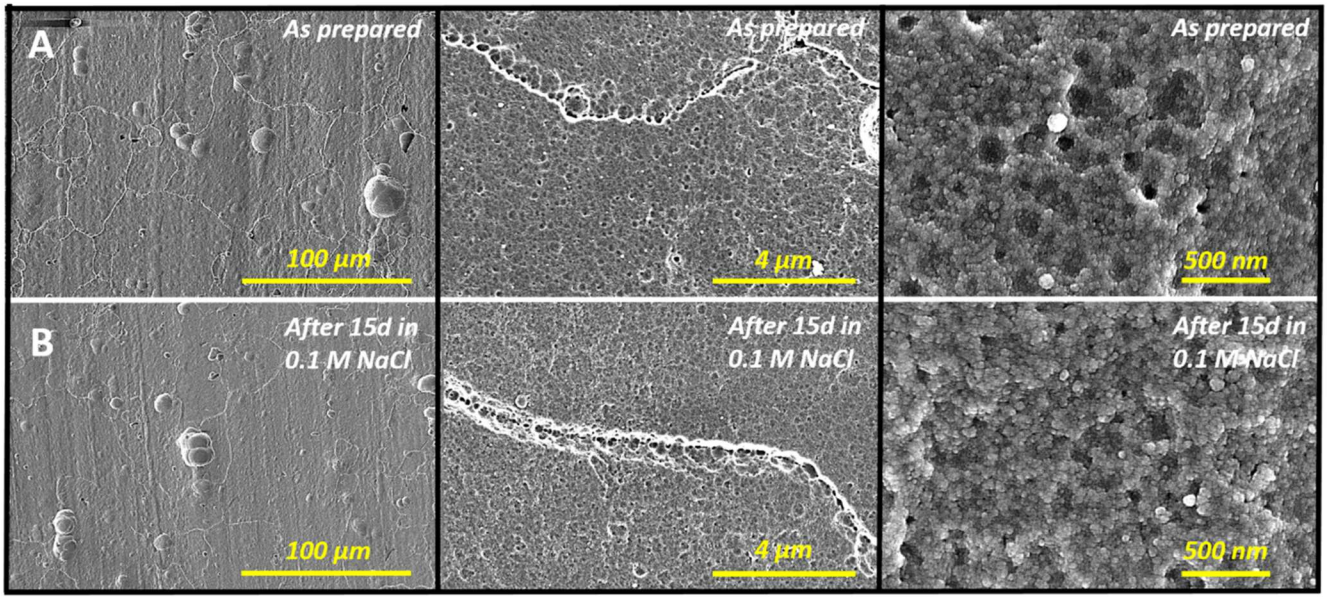

Figure 15. SEM-SE images of ZrCC applied on AA7075 samples after commercial surface pretreatment CP1. (a) as prepared ZrCC, (b) after 15 days of immersion in 0.1 M NaCl solution. * No corrosion damage was observed on the sample after 15 days of immersion (CP1-A*-ZrCC). EDS analysis is presented in Table II.

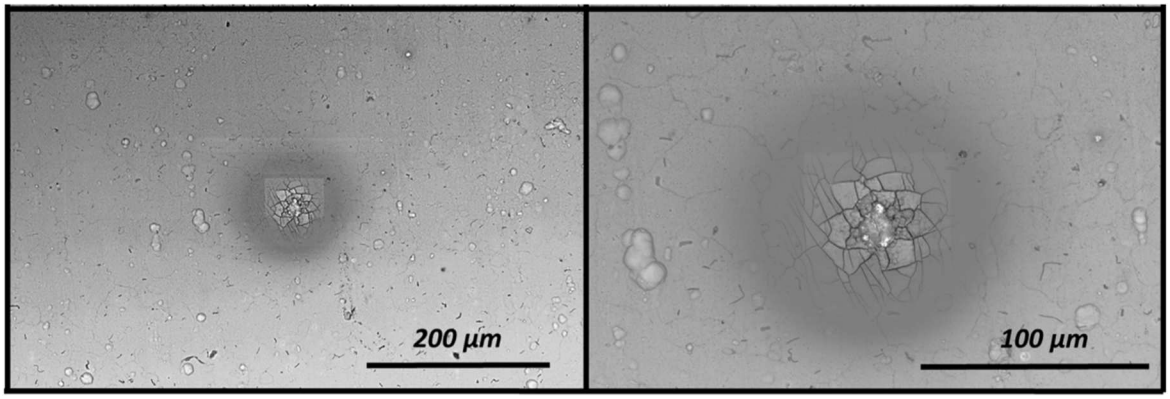

Figure 16. SEM-SE images of ZrCC applied on AA7075 samples after commercial surface pretreatment CP1, after 15 days of immersion in 0.1 M NaCl solution. * The corrosion damage of the sample was in the form of a single pit after 15 days of immersion (CP1-B**-ZrCC). EDS analysis is presented in Table II.

Microstructural and spectroscopic analyses confirmed a corrosion-induced self-sealing mechanism in CP1-ZrCC after 15 days of immersion in 0.1 M NaCl. SEM-EDS and XPS revealed surface fluorine depletion and oxygen enrichment, indicating formation of protective Al-oxide/hydroxide phases. XPS data supported this, showing complete loss of F 1 s, an O 1 s shift to 532.0 eV, and Zr 3 d transitions consistent with conversion from ZrF_4/ZrO_xF_y to hydrated ZrO_2 and $Al(OH)_3$. ToF-SIMS detected no loss in coating thickness but revealed sulfur migration toward the interface and a 10 nm shift of the AlO^- signal, suggesting interfacial densification and sulfur incorporation. The loss of fluorine from the outer layer was also noted. These observations confirm the self-sealing mechanism from our previous work[23,34,58,78] and collectively demonstrate the dynamic chemical and structural adaptation of CP1-ZrCC, underpinning its enhanced durability in chloride-rich environments.

It should be noted that ToF-SIMS profiles reveal that the superior corrosion resistance and self-sealing ability of CP1-ZrCC are not related to the coating thickness in a simple manner. Despite being the thinnest (∼40 nm), CP1-ZrCC exhibited the most compact, uniform structure and best performance (Figs. 1–3, 6), contradicting the assumption that thicker coatings offer better protection. The incorporation of sulfur in the top layer likely contributed to its enhanced corrosion resistance.

Collectively, these findings emphasise the importance of an optimised chemical pretreatment strategy that promotes selective dealloying, oxide layer compaction, and the favourable incorporation of trace elements from AA7075-T6 and other 7xxx alloys. Furthermore, integrating microstructural and electrochemical analyses is essential for revealing the actual protective mechanisms of Zr-based conversion coatings, particularly under long-term exposure conditions.

Conclusions

The rationale for the present study was to evaluate how acidic, alkaline, and commercial pretreatments affect the properties of zirconium conversion coatings deposited on aluminium alloy 7075-T6 and their impact on the corrosion performance.

1. Zirconium conversion coating applied after commercial SurTec® pretreatment (CP1-ZrCC) showed remarkable corrosion resistance with an active, self-sealing corrosion protection effect,

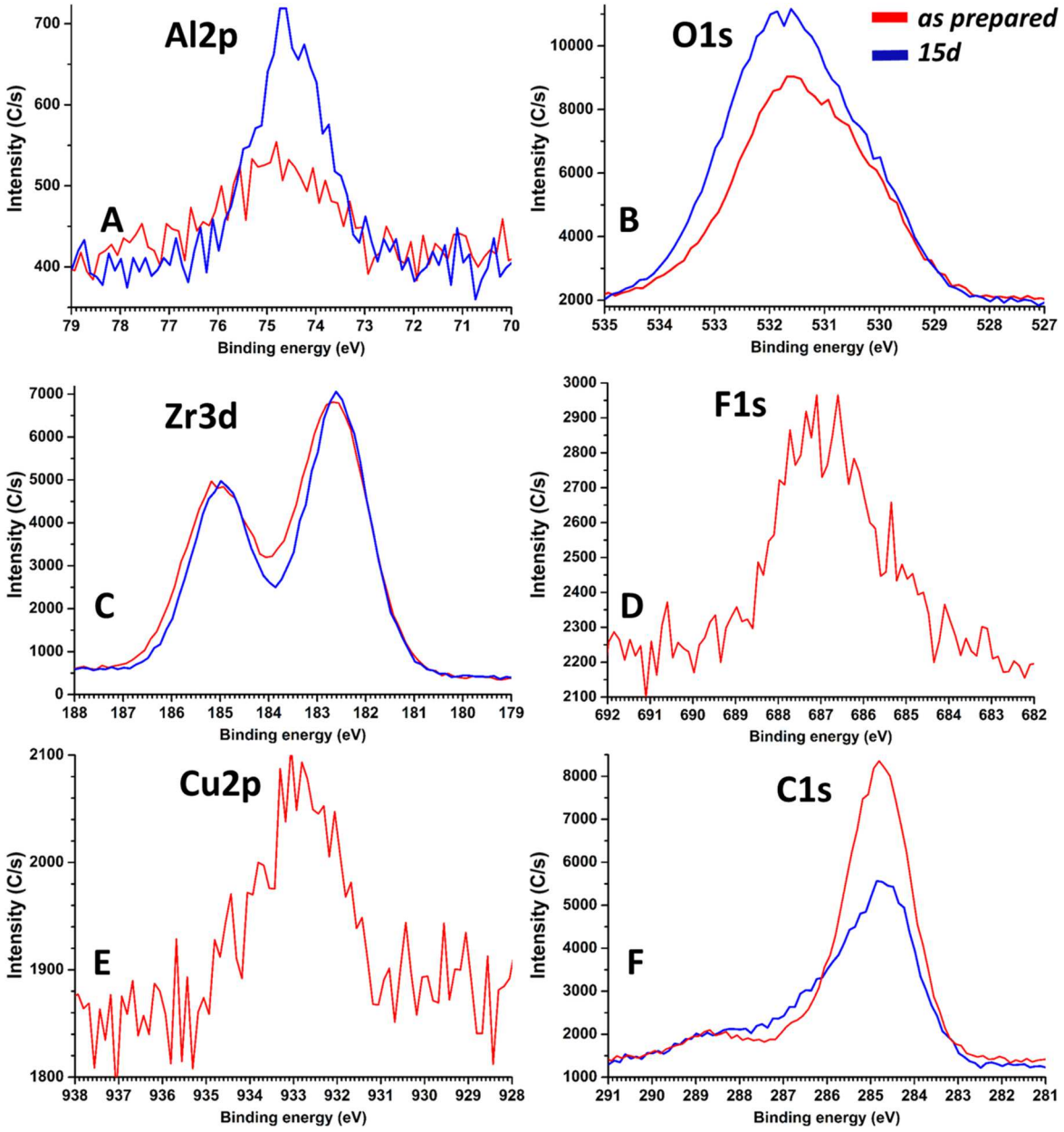

Figure 17. High energy resolution XPS spectra of (a) Al 2p, (b) O 1s, (c) Zr 3 d, (d) F 1s, (e) Cu $2p_{3/2}$, and C 1s for ZrCC applied on AA7075 sample after commercial surface pretreatment CP1. The red line denotes the as-prepared CP1-ZrCC, and the blue line the CP1-ZrCC after 15 days of immersion in 0.1 M NaCl solution. Spectra were not normalized on the intensity scale. * No corrosion damage was observed on the sample after 15 days of immersion (CP1-A*-ZrCC) (Table III).

which almost reached the level of trivalent chromium process (TCP) conversion coating applied after the same pretreatment.

2. Commercial pretreatment CP1 produced the most compact, uniform, and thinnest aluminium oxide layer (10 nm) with visible grain boundaries. It almost completely removed Mg from the alloy's surface, leaving trace contents of F, Si, Mg, Cu, Zn, N, and S.
3. CP1-ZrCC had a bilayer structure with a thickness of about 40 nm. The upper layer predominantly comprised ZrO_2, while AlO_xF_y and aluminium oxide dominated the lower layer. Sulphur was part of ZrCC and followed the distribution of the ZrO_2 layer.
4. Microstructural analysis of as-prepared CP1-ZrCC and CP1-ZrCC-15d after 15 days of immersion in 0.1 M NaCl supports our previously proposed self-sealing mechanism. In this process, the release of F from CP1-ZrCC, coupled with an increase in O concentration, drives the compositional transformation from ZrF_4/ZrO_xF_y to $ZrO_2{\cdot}xH_2O$ while facilitating pore sealing through the formation of $Al(OH)_3$. This evolution enhances corrosion resistance.
5. Zirconium conversion coatings formed following various non-commercial pretreatments exhibited a bilayer structure, except in the cases of strong alkaline etching (CP4) and pseudoboehmite (CP9) pretreatments. For these two pretreatments, the ZrCC was deposited atop the pre-existing pseudoboehmite and aluminium/magnesium hydroxide layers. Corrosion protection was unsatisfactory after these pretreatments.
6. Surface pretreatment CP13, which followed the same procedural steps as CP1 but with the desmutting agent replaced by HNO_3 within the same pH range, resulted in significantly reduced corrosion resistance of the applied conversion coating (CP13-ZrCC). This finding highlights the critical role of the desmutting process in chemical pretreatments.

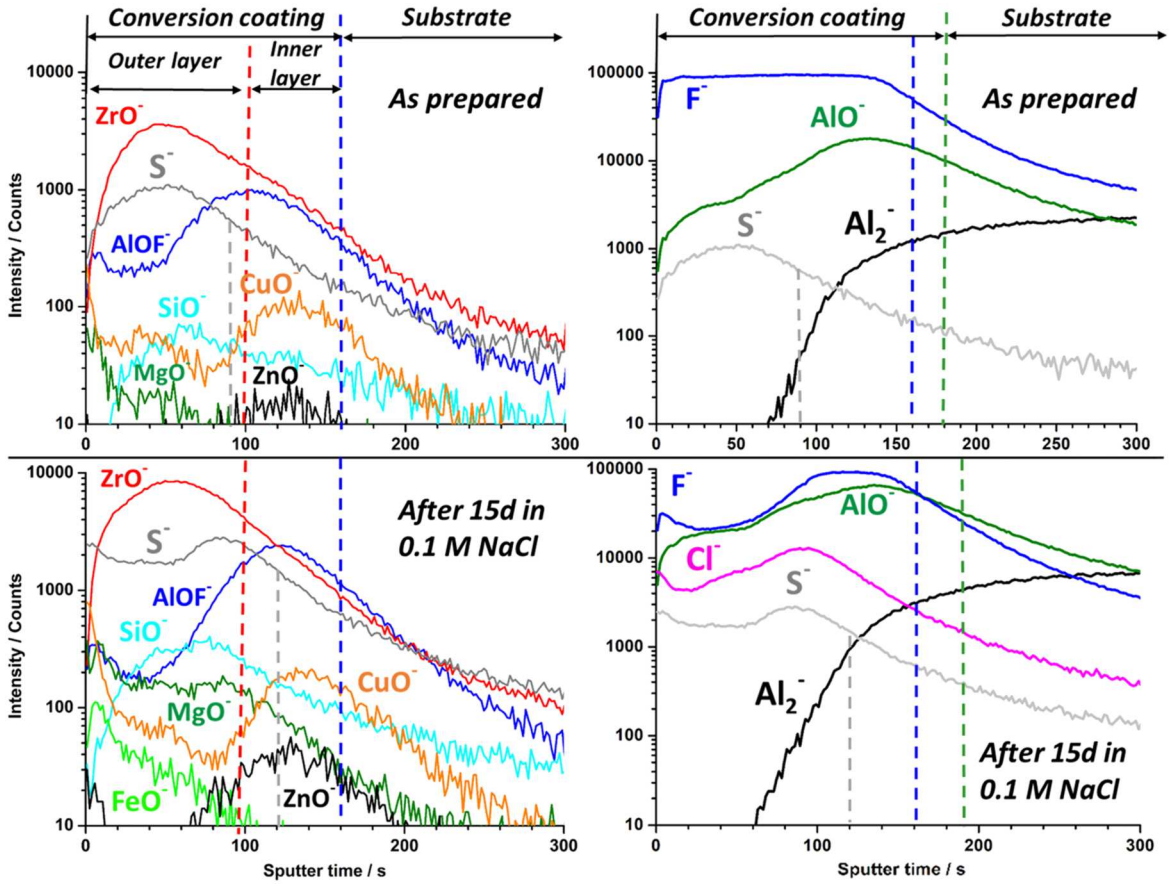

Figure 18. ToF-SIMS negative-ion profiles of ZrCC applied on the AA7075 sample after commercial surface pretreatment CP1. (a) as prepared ZrCC (b) after 15 days of immersion in 0.1 M NaCl solution. * No corrosion damage was observed on the sample after 15 days of immersion (CP1-A*-ZrCC) (Table II). The sputtering rate was 0.3 nm s^{-1}. The thickness values are presented in Table V.

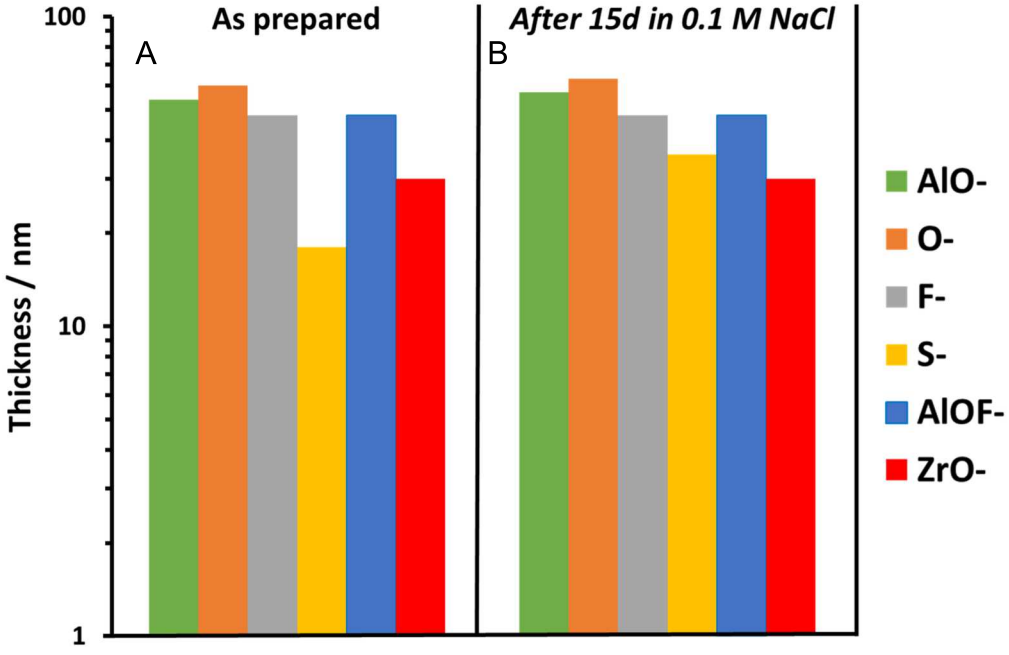

Figure 19. The thickness of ToF-SIMS negative-ion profiles for zirconium conversion coating applied on AA7075 after commercial surface pretreatment CP1. (a) as prepared ZrCC, (b) after 15 days of immersion in 0.1 M NaCl solution. * No corrosion damage was observed on the sample after 15 days of immersion (CP1-A*-ZrCC) (Table II).

Table V. The thickness of negative-ion profiles for as-prepared CP1-ZrCC-coated and after immersion for 15 days in 0.1 M NaCl solution (CP1-A*-ZrCC-15d). The thickness of negative-ion profiles was determined as the depth at which the intensity of negative ions dropped to a half value of their maximum values (Fig. 19). Sputtering rate was 0.3 nm s^{-1}.

Sample	AlO^-	O_2^-	F^-	$AlOF^-$	ZrO^-	S^-
CP1-ZrCC	54 nm	60 nm	48 nm	48 nm	30 nm	24 nm
CP1-ZrCC-15d	57 nm	63 nm	48 nm	48 nm	30 nm	40 nm

Acknowledgments

The authors thank Tatjana Filipič, MSc, for XPS and ToF-SIMS measurements (Department of Surface Engineering, Jožef Stefan Institute). The Centre of Excellence in Nanoscience and Nanotechnology—Nanocentre, Ljubljana, is acknowledged for the use of the FEI Helios Nanolab 650 microscope.

Funding

The authors acknowledge the funding from the Slovenian Research and Innovation Agency (core funding grant numbers PR-07023, P2–0393 and P2–0082).

ORCID

Gavrilo Šekularac https://orcid.org/0000-0002-6370-4983
Janez Kovač https://orcid.org/0000-0002-4324-246X
Ingrid Milošev https://orcid.org/0000-0002-7633-9954

References

1. C. Vargel, *Corrosion of Aluminium* (Elsevier Science, Oxford, UK) 1st ed. (2004).
2. J. R. Davis, *Corrosion of Aluminum and Aluminum Alloys* (ASM International, USA) (1999).
3. Z. Szklarska-Smialowska, *Corros. Sci.*, **41**, 1743 (1999).
4. Z. Szklarska-Smialowska, *Corros. Sci.*, **44**, 1143 (2002).
5. N. Birbilis, M. K. Cavanaugh, and R. G. Buchheit, *Corros. Sci.*, **48**, 4202 (2006).
6. N. Birbilis and R. G. Buchheit, *J. Electrochem. Soc.*, **152**, B140 (2005).
7. J. Li, N. Birbilis, and R. G. Buchheit, *Corros. Sci.*, **101**, 155 (2015).
8. Y. Zhu, K. Sun, and G. S. Frankel, *J. Electrochem. Soc.*, **165**, C807 (2018).
9. I. Milošev and G. S. Frankel, *J. Electrochem. Soc.*, **165**, C127 (2018).
10. A. E. Hughes, J. M. C. Mol, M. L. Zheludkevich, and R. G. Buchheit, *Active Protective Coatings* (Springer, Dordrecht) 428 (2016).
11. S. T. Abrahami, J. M. M. de Kok, H. Terryn, and J. M. C. Mol, *Front. Chem. Sci. Eng.*, **11**, 465 (2017).
12. P. Rodič, B. Kapun, and I. Milošev, *Npj Mater. Degrad.*, **8**, 58 (2024).
13. G. M. Brown, K. Shimizu, K. Kobayashi, G. E. Thompson, and G. C. Wood, *Corros. Sci.*, **35**, 253 (1993).
14. M. W. Kendig and R. G. Buchheit, *Corrosion*, **59**, 379 (2003).
15. N. Banjo, T. T. Sasaki, and K. Hono, *Appl. Surf. Sci.*, **604**, 154411 (2022).
16. O. Gharbi, S. Thomas, C. Smith, and N. Birbilis, *Npj Mater. Degrad.*, **2**, 12 (2018).
17. F. Peltier and D. Thierry, *Coatings*, **12**, 518 (2022).
18. J. T. Qi, T. Hashimoto, J. R. Walton, X. Zhou, P. Skeldon, and G. E. Thompson, *Surf. Coat. Technol.*, **280**, 317 (2015).
19. E. Gralak, J. Szczepańska, K. Winiarska, W. Tylus, and J. Winiarski, *Mater. Today Commun.*, **38**, 108409 (2024).
20. M. Nabizadeh, K. Marcoen, T. Kolberg, D. Schatz, H. Terryn, and T. Hauffman, *Surf. Coat. Technol.*, **441**, 128567 (2022).
21. A. Kraš and I. Milošev, *Electrochim. Acta*, **502**, 144819 (2024).
22. A. Kraš, D. Kramar, and I. Milošev, *Corros. Sci.*, **249**, 112824 (2025).
23. M. Mujdrica Kim, B. Kapun, and I. Milošev, *J. Electrochem. Soc.*, **172**, 061501 (2025).
24. Y.-T. Wu, S.-Y. Chen, Z.-S. Yang, H.-S. Huang, I. C. Cheng, and C.-S. Lin, *Corros. Sci.*, **256**, 113188 (2025).
25. C. A. Munson and G. M. Swain, *Surf. Coat. Technol.*, **315**, 150 (2017).
26. L. Li, K. P. Doran, and G. M. Swain, *J. Electrochem. Soc.*, **160**, C396 (2013).
27. M. Ely, J. Światowska, A. Seyeux, S. Zanna, and P. Marcus, *J. Electrochem. Soc.*, **164**, C276 (2017).
28. L. Li, G. P. Swain, A. Howell, D. Woodbury, and G. M. Swain, *J. Electrochem. Soc.*, **158**, C274 (2011).
29. J. Qi, J. Światowska, P. Skeldon, and P. Marcus, *Corros. Sci.*, **167**, 108482 (2020).
30. J. Qi, L. Gao, Y. Li, Z. Wang, G. E. Thompson, and P. Skeldon, *J. Electrochem. Soc.*, **164**, C390 (2017).
31. J. Qi, T. Hashimoto, J. Walton, X. Zhou, P. Skeldon, and G. E. Thompson, *J. Electrochem. Soc.*, **163**, C25 (2016).
32. Y. Guo and G. S. Frankel, *Surf. Coat. Technol.*, **206**, 3895 (2012).
33. N. W. Khun and G. S. Frankel, *Corrosion*, **71**, 277 (2014).
34. G. Šekularac, J. Kovač, and I. Milošev, *Corros. Sci.*, **169**, 108615 (2020).
35. N. W. Khun, S. Adhikari, Y. Y. Li, G. S. Frankel, J. McGee, T. Smith, B. Bammel, and J. Zimmerman, *Corrosion*, **73**, 339 (2016).
36. I. Schoukens, I. Vandendael, J. De Strycker, A. A. Saleh, H. Terryn, and I. De Graeve, *Surf. Coat. Technol.*, **235**, 628 (2013).
37. A. Sarfraz, R. Posner, M. M. Lange, K. Lill, and A. Erbe, *J. Electrochem. Soc.*, **161**, C509 (2014).
38. J. Han, D. Thierry, and K. Ogle, *Surf. Coat. Technol.*, **402**, 126236 (2020).
39. S. Adhikari, K. A. Unocic, Y. Zhai, G. S. Frankel, J. Zimmerman, and W. Fristad, *Electrochim. Acta*, **56**, 1912 (2011).
40. X. Liu et al., *ACS Appl. Nano Mater.*, **2**, 1920 (2019).
41. M. Mujdrica Kim, B. Kapun, U. Tiringer, G. Šekularac, and I. Milošev, *Coatings*, **9**, 563 (2019).
42. F. Andreatta, A. Lanzutti, L. Paussa, and L. Fedrizzi, *Prog. Org. Coat.*, **77**, 2107 (2014).
43. G. Yoganandan, K. Pradeep Premkumar, and J. N. Balaraju, *Surf. Coat. Technol.*, **270**, 249 (2015).
44. F. Andreatta, A. Turco, I. De Graeve, H. Terryn, J. H. W. De Wit, and L. Fedrizzi, *Surf. Coat. Technol.*, **201**, 7668 (2007).
45. M. D. Havigh, M. Nabizadeh, B. Wouters, N. Hallemans, T. Hauffman, J. Lataire, A. Hubin, and H. Terryn, *Corros. Sci.*, **223**, 111469 (2023).
46. A. Kraš, I. Milošev, A. Seyeux, and P. Marcus, *Npj Mater. Degrad.*, **8**, 65 (2024).
47. O. Lunder, C. Simensen, Y. Yu, and K. Nisancioglu, *Surf. Coat. Technol.*, **184**, 278 (2004).
48. J. H. Nordlien, J. C. Walmsley, H. Østerberg, and K. Nisancioglu, *Surf. Coat. Technol.*, **153**, 72 (2002).
49. L. Li, A. L. Desouza, and G. M. Swain, *Analyst*, **138**, 4398 (2013).
50. A. Kraš and I. Milošev, *J. Electrochem. Soc.*, **170**, 021508 (2023).
51. M. Doerre, L. Hibbitts, G. Patrick, and K. N. Akafuah, *Coatings*, **8**, 405 (2018).
52. U. Tiringer, J. P. B. Van Dam, S. T. Abrahami, H. Terryn, J. Kovač, I. Milošev, and J. M. C. Mol, *Surf. Interfaces*, **26**, 101417 (2021).
53. H. R. Asemani, P. Ahmadi, A. A. Sarabi, and H. Eivaz Mohammadloo, *Prog. Org. Coat.*, **94**, 18 (2016).
54. N. W. Khun, G. S. Frankel, and J. Zimmerman, *Corrosion*, **69**, 259 (2012).
55. E. Mysliu, K. S. Storli, H. M. Skogøy, S. Kubowicz, I.-H. Svenum, O. Lunder, and A. Erbe, *Electrochim. Acta*, **477**, 143805 (2024).
56. M. Eslami, V. Pachchigar, M. Sankaran, and D. V. Krogstad, *Appl. Surf. Sci.*, **697**, 163018 (2025).
57. J. J. Alba-Galvín, L. González-Rovira, F. J. Botana, M. Lekka, F. Andreatta, L. Fedrizzi, and M. Bethencourt, *Metals*, **11**, 930 (2021).
58. G. Šekularac, J. Kovač, and I. Milošev, *J. Electrochem. Soc.*, **167**, 111506 (2020).
59. U. Tiringer, J. Kovač, and I. Milošev, *Corros. Sci.*, **119**, 46 (2017).
60. J. Qi, A. Němcová, J. R. Walton, X. Zhou, P. Skeldon, and G. E. Thompson, *Thin Solid Films*, **616**, 270 (2016).
61. C. F. Glover, M. L. C. Lim, G. Post, M. Mayo, and J. R. Scully, *Corrosion*, **75**, 1513 (2019).
62. W. Pinc, S. Geng, M. O'keefe, W. Fahrenholtz, and T. O'keefe, *Appl. Surf. Sci.*, **255**, 4061 (2009).
63. X. Verdalet-Guardiola, R. Saillard, B. Fori, S. Duluard, and C. Blanc, *Corros. Sci.*, **167**, 108508 (2020).
64. L. Li, A. L. Desouza, and G. M. Swain, *J. Electrochem. Soc.*, **161**, C246 (2014).
65. I. Milošev and P. Rodič, *J. Electrochem. Soc.*, **169**, 011504 (2022).
66. N. Banjo, T. T. Sasaki, and K. Hono, *Appl. Surf. Sci.*, **661**, 160005 (2024).
67. A. De Frutos, M. A. Arenas, Y. Liu, P. Skeldon, G. E. Thompson, J. De Damborenea, and A. Conde, *Surf. Coat. Technol.*, **202**, 3797 (2008).
68. S. Joshi, W. G. Fahrenholtz, and M. J. O'Keefe, *Appl. Surf. Sci.*, **257**, 1859 (2011).
69. M. Li, Y. Ma, J. Yan, M. Ma, L. Wu, and H. Wu, *J. Electrochem. Soc.*, **171**, 111501 (2024).
70. G.-T. Shen, S.-Y. Chen, C.-Y. Huang, and C.-S. Lin, *Appl. Surf. Sci.*, **635**, 157657 (2023).
71. P. Zhou, Y. Liu, L. Liu, B. Yu, T. Zhang, and F. Wang, *Surf. Coat. Technol.*, **377**, 124904 (2019).
72. J. Cerezo, P. Taheri, I. Vandendael, R. Posner, K. Lill, J. H. W. de Wit, J. M. C. Mol, and H. Terryn, *Surf. Coat. Technol.*, **254**, 277 (2014).
73. J. Cerezo, I. Vandendael, R. Posner, J. H. W. de Wit, J. M. C. Mol, and H. Terryn, *Appl. Surf. Sci.*, **366**, 339 (2016).
74. J. Cerezo, I. Vandendael, R. Posner, K. Lill, J. H. W. De Wit, J. M. C. Mol, and H. Terryn, *Surf. Coat. Technol.*, **236**, 284 (2013).
75. S.-Y. Chen, C.-Y. Huang, and C.-S. Lin, *Corros. Sci.*, **184**, 109354 (2021).
76. B. B. M. Sultan, D. Persson, D. Thierry, J. Han, and K. Ogle, *Electrochim. Acta*, **503**, 144820 (2024).
77. C. F. Glover, M. L. C. Lim, and J. R. Scully, *Corrosion*, **77**, 40 (2021).
78. G. Šekularac and I. Milošev, *J. Electrochem. Soc.*, **167**, 021509 (2020).
79. NACE TM0169/G31-12a, *Standard Guide for Laboratory Immersion Corrosion Testing of Metals 1* (AMPP The Association for Materials Protection and Performance, Houston, TX) (2012).
80. ASTM International, G 59–97, *Standard Test Method for Conducting Potentiodynamic Polarization Resistance Measurements* (ASTM International, West Conshohocken, PA, USA) (1998).
81. N. Birbilis, R. G. Buchheit, and M. K. Cavanaugh, *ECS Trans.*, **1**, 115 (2006).
82. J. van den Brand, W. G. Sloof, H. Terryn, and J. H. W. de Wit, *Surf. Interface Anal.*, **36**, 81 (2004).
83. E. McCafferty and J. P. Wightman, *Surf. Interface Anal.*, **26**, 549 (1998).
84. I. Milošev, H. H. Strehblow, and B. Navinšek, *Surf. Interface Anal.*, **26**, 242 (1998).
85. X. Dou, D. Mohan, C. U. Pittman Jr, and S. Yang, *Chem. Eng. J.*, **198**, 236 (2012).